

1 **OH-initiated aqueous photooxidation of smoke extracts from maize**
2 **straw and coal combustion: optical properties and molecular**
3 **composition**

4 Zhaolian Ye¹, Dandan Hu¹, Qiuyan Chen¹, Xiangpeng Huang¹, Xinlei Ge²

5 ¹ School of Resources and Environmental Engineering, Jiangsu University of
6 Technology, Changzhou 213001, China

7 ² School of Energy and Environment, Southeast University, Nanjing, 211189, China.

8 Correspondence: Zhaolian Ye (bess_ye@jsut.edu.cn) and Xinlei Ge
9 (xinlei@seu.edu.cn)

10 **Abstract:** Aqueous-phase •OH photodegradation of coal- and maize-derived smoke
11 extracts was investigated to elucidate their optical and molecular transformations.
12 Parallel factor analysis of excitation-emission matrix fluorescence spectra identified
13 one humic-like and two protein-like substances. FT-ICR MS revealed that CHO
14 (74.5% for maize, 58.9% for coal) and CHON (24.1% for maize, 11.8% for coal)
15 compounds dominated both smoke extracts, whereas sulfur-containing species were
16 more abundant in coal smoke (29.4%) than in maize (1.4%). The aqueous •OH
17 photooxidation enhanced molecular saturation and reduced aromaticity, reflected by
18 lower double bond equivalent and aromaticity index values. The abundance of
19 lignin-like compounds decreased, whereas lipid- and aliphatic-like fractions increased,
20 suggesting a transformation of aromatic species into more saturated products, which
21 correspondingly reduced light absorption and overall fluorescence intensity. Distinct
22 photodegradation pathways were observed for coal and maize extracts based on
23 changes in resistant, degraded, and newly formed molecules. Reactive species

24 contributed to WSOC degradation in the order $\bullet\text{OH} > {}^3\text{C} > {}^1\text{O}_2$, with contributions of
25 86.4%, 12.8%, and 0.8% for coal extracts, and 80.9%, 16.0%, and 3.1% for maize
26 extracts, respectively. Increased oxalic acids, CHO_2^+ fragments, and declining pH
27 values during the first 5 h indicated substantial formation of carboxylic acids.
28 Measurements from aerosol mass spectrometry showed increasing oxidation
29 indicators during this early stage, confirming enhanced oxidation of aqueous
30 secondary organic aerosol. Oxidative potential, assessed by dithiothreitol
31 consumption, initially increased and then declined, while its normalization by
32 water-soluble organic carbon increased, likely due to the formation of
33 nitrogen-containing compounds in coal smoke and reactive quinones in maize smoke,
34 respectively. Overall, this study improves understanding of aqueous-phase
35 photochemical processing of smoke-derived water-soluble organic matter and
36 supports more accurate representation of these processes in atmospheric models,
37 contributing to better assessments of smoke aging impacts on air quality and climate.

38 **Keywords:** molecular transformations, optical characteristic, FT-ICR MS, reactive
39 species, dithiothreitol (DTT) consumption rate

40

41 **1 Introduction**

42 The atmospheric aqueous phase contains a variety of oxidants, such as hydrogen
43 radical ($\bullet\text{OH}$), peroxy radicals, singlet oxygen (${}^1\text{O}_2$), and excited triplet states of
44 organic compounds (${}^3\text{C}^*$), which can trigger aqueous-phase oxidation reaction.
45 Aqueous-phase process has been recognized as a significant source of secondary
46 organic aerosol (SOA) and key contributors to light-absorbing compounds, thereby

47 influencing radiative forcing and air quality (Arciva et al., 2024; Go et al., 2023).
48 Extensive studies have investigated the chemical composition, light-absorption
49 properties, and SOA mass yield from single-component model compounds (Arciva et
50 al., 2022; Li et al., 2022). Recently, increasing attention has been toward the aqueous
51 photoaging of complex mixtures, including laboratory-generated SOA or
52 multicomponent systems (Gerritz et al., 2024; Go et al., 2024). Moreover, studies on
53 aqueous aging of water-soluble organic matter (WSOM) derived from actual smoke
54 particle or PM_{2.5} extracts provide valuable insights into aqueous-phase processing
55 under more realistic atmospheric conditions (Fan et al., 2018; Hems et al., 2020;
56 Wong et al., 2017). Organic matter (OM) within smoke particles, which accounts for
57 up to 60-90% of total mass, is a complex mixture of aromatic and aliphatic
58 compounds with diverse functional groups. The chemical complexity of these
59 precursors poses challenges for comprehensive product characterization and
60 mechanistic studies. Molecular-level compositional data are therefore crucial for
61 improving our understanding of the role of smoke-derived OM in atmospheric
62 aqueous-phase chemistry. High-resolution mass spectrometry (MS) techniques with
63 soft ionization methods, such as Fourier transform ion cyclotron resonance mass
64 spectrometry (FT-ICR MS), enable detailed molecular characterization in complex
65 mixtures and have been widely applied in aerosol studies (Cao et al., 2025; Wang et
66 al., 2017).

67 To date, only a few studies (Leresche et al., 2021; Lei et al., 2024) have
68 examined photochemical aging characteristics of aqueous extracts of smoke particles
69 or atmospheric fine particulate matter, most of which have appeared only recently.
70 Notably, few investigations have compared the molecular and optical changes during
71 aqueous-phase oxidation of smoke extracts from different fuel sources. Cao et al.

72 (2025) compared molecular-level composition and fluorophore changes of extracted
73 WSOM, but their study did not consider the distinct contributions of various reactive
74 oxygen species (ROS) to the oxidation process. Additionally, the wavelength of the
75 light source can significantly influence the photochemical reactivity of organic
76 compounds. For instance, syringaldehyde was found to inhibit the degradation of
77 vanillyl alcohol under UV-B irradiation due to light-absorbing competition, whereas it
78 promoted the degradation of vanillyl alcohol under UV-A irradiation via the
79 photosensitization effect of syringaldehyde (Li et al., 2024).

80 To elucidate the reaction mechanism involved in aqueous-phase photooxidation,
81 it is crucial to understand the formation, transformation, and roles of ROS during
82 photolysis. Biomass burning smoke—such as that produced from agricultural crop
83 residues—contains a variety of potential organic photosensitizers bearing with
84 carbonyl groups and conjugated double bonds, which can absorb sunlight and
85 generate ROS (e.g., $\text{HO}_2/\text{O}_2^{\cdot-}$, $^1\text{O}_2$, $\text{C}\alpha\text{OH}$), thereby enhancing atmospheric oxidative
86 capacity. However, direct quantification of ROS remains challenging (Gerritz et al.,
87 2024; Leresche et al., 2021; Manfrin et al., 2019). For instance, Gerritz et al. (2024)
88 investigated the photolytic formation of ROS in aqueous extracts of
89 laboratory-generated SOA using an in situ UV-vis irradiation system coupled with
90 electron paramagnetic resonance (EPR) spectroscopy and identified organic peroxides
91 and carbonyls as major ROS precursors. Manfrin et al. (2019) reported the $^1\text{O}_2$
92 formation from photosensitized reactions mediated by aromatic SOA, although free
93 radicals were not directly measured. Due to the chemical complexity of
94 smoke-derived WSOM and the analytical difficulty in quantifying ROS, the
95 underlying reaction mechanisms remain poorly understood.

96 Further investigation into the aqueous photoaging of WSOM from different

97 combustion sources is crucial to understanding the underlying mechanisms driving
98 chemical transformation and light absorption. Comparative studies of maize- and
99 coal-derived WSOM under simulated sunlight can reveal how source-dependent
100 compositions influence photo-reactivity and light-absorbing compounds formation.
101 This study compares the optical, molecular evolution and oxidative potential of maize
102 (a representative agricultural residue) and coal smoke extracts during OH-induced
103 photooxidation. WSOM from both smoke types were analyzed using UV-vis
104 spectrometer, excitation-emission matrix (EEM) fluorescence, and FT-ICR MS to
105 identify similarities and differences in photoaging behavior. High-resolution
106 time-of-flight aerosol mass spectrometers (HR-AMS) were used to characterize the
107 bulk chemical composition of low-volatility organics (denoted as aqSOA) over
108 photoreaction. Our findings will provide insights into the chemical evolution and
109 environmental impacts of smoke-derived organic matter.

110

111 **2 Materials and Methods**

112 **2.1 Chemicals and solutions**

113 The following reagents were purchased from the Sigma-Aldrich
114 (dithiothreitol, >99%; 5,5'-dithiobis (2-nitrobenzoic acid), >99%; benzoic acid, >99%;
115 syringol, >99%; furfuryl alcohol, >99%). Methanol ($\geq 99\%$), acetonitrile ($\geq 99\%$),
116 Na_2CO_3 ($\geq 99\%$) and NaHCO_3 ($\geq 99\%$) were purchased from Acros Chemicals.
117 Sulfuric acid ($\geq 99\%$) was obtained from Sinopharm. $(\text{NH}_4)_2\text{SO}_4$ (GR), H_2O_2
118 (29%~32%) and KOH($\geq 99\%$) were supplied by Aladdin and Alfa Aesar, respectively.
119 2,2,6,6-Tetramethylpiperidine ($\geq 98\%$) and 5,5-dimethyl-1-pyrroline N-oxide ($\geq 97\%$)

120 were purchased from Anpel Laboratory Technologies (Shanghai) Co., Ltd.

121 All chemicals were used as received without further purification. All solutions
122 were prepared with ultrapure water (resistivity \geq 18.2 M Ω cm) produced by a Milli-Q
123 purification system.

124 **2.2 Sample collection and experiment preparation**

125 Coal and maize straw were collected from Lingwu (Ningxia) and Shangqiu
126 (Henan Province), respectively, and combusted in a self-built stove designed to
127 simulate domestic fuel burning conditions. Smoke particle collection followed the
128 procedures described in our previous study (Ye et al., 2025). Briefly, the stove was
129 connected to a stainless steel dilution tunnel and residence chamber. Smoke particles
130 emitted from maize straw and coal combustion were collected on pre-baked quartz
131 fiber filters (20.3 \times 25.4 cm, Whatman) using two samplers equipped with cyclone
132 with a 2.5 μ m aerodynamic cutoff.

133 One quarter of each filter was cut into strips and placed in extraction bottles. The
134 samples were ultrasonically extracted three times with 30 mL Milli-Q water. The
135 combined extracts were filtered through a 0.45 μ m PTFE membrane and subsequently
136 diluted to approximately 15 mgC/L for photoaging experiment based on suggested
137 TOC level (0.5-1.4 mmol C/L) by Cook et al. (2017) for cloud water. Photochemical
138 reactions were performed in a Rayonet RPR-200 photoreactor equipped with 14
139 lamps, following the procedure described in our previous study (Ye et al., 2025). The
140 irradiance intensity on the solution surface was 2.4 mW/cm² in the wavelength region
141 of 290-400 nm (centered at 313 nm), as measured by a radiometer (Photoelectric
142 Instrument Factory of Everfine Corporation, Hangzhou, China). The intensity is slight

143 lower than natural sunlight levels (6.16 mW/cm²) measured at noon during winter at
144 Jiangsu University of Technology (Wang et al., 2025). Before photooxidation, 10 mM
145 H₂O₂ was added to the reaction solution to generate $\cdot\text{OH}$ with certain concentration,
146 consistent with previous study (Arciva et al., 2022; Cao et al., 2025).

147 **2.3 Chemical analysis**

148 Water-soluble organic carbon (WSOC) concentrations were determined using a
149 total organic carbon (TOC) analyzer (TOC-L CPH, Shimadzu, Japan). Metal element
150 concentrations (Fe and Cu) were quantified by inductively coupled plasma-mass
151 spectrometry (ICP-MS, Agilent 7800). Eight water soluble inorganic ions (Na⁺, Cl⁻,
152 SO₄²⁻, NO₃⁻, K⁺, NH₄⁺, Ca²⁺ and Mg²⁺) were also detected for both smoke extracts.
153 Details can be found in Sect. S1 in the Supplement. These detection limits were
154 determined based on three times the standard deviation of blank sample. The method
155 detection limits ranged from 5-20 $\mu\text{g/L}$ for anions and 0.5-2 $\mu\text{g/L}$ for cations. The
156 detection limits of Fe and Cu are 2.0 $\mu\text{g/L}$ and 0.8 $\mu\text{g/L}$, respectively.

157 **2.4 UV-vis and EEM analysis**

158 The UV-vis absorption spectra were monitored using UV-vis spectrophotometer
159 (Shimadzu, Japan) over wavelength range of 200-700 nm. The mass absorption
160 coefficients (MACs, m²/gC), defined as absorbance normalized by WSOC
161 concentration, were calculated as follows:

$$162 \quad \text{MAC}_\lambda = \frac{A_\lambda}{C \times L} \times \ln 10 \quad (1)$$

163 Where A_λ represent the absorbance at wavelength λ . C refers to the WSOC
164 concentration of reaction solution. L is the optical path length (1 cm in this study).

165 The EEM spectra were recorded using a three-dimensional fluorescence

166 spectrophotometer (FluoroMax Plus, HORIBA Scientific). Parallel factor analysis
167 (PARAFAC) model was applied to EEM spectra to resolve the fluorescent compounds
168 using the DOMFluor toolbox in MATLAB 2021b. Details of the determination and
169 modeling procedures are provided in our previous study (Ye et al., 2025). Three
170 fluorescence components (C1, C2 and C3) were identified from PARAFAC model.
171 The fluorescence index (FI), humification index (HIX), and biological index (BIX)
172 were further calculated to characterize the fluorescent properties of the samples. The
173 calculation methods for these indicators were shown in the supplement and in our
174 previous study (Ye et al., 2025).

175 **2.5 FT-ICR MS measurement**

176 The molecular compositions, degree of unsaturation, and aromaticity of WSOM
177 were characterized using FT-ICR MS coupled with negative electrospray ionization
178 (ESI-). Solid-phase extraction (SPE) was employed for sample pretreatment prior to
179 FT-ICR MS determination, following procedures similar to those described in
180 previous studies (Yang et al., 2025). Briefly, the reaction solution was adjusted to pH
181 2 and pass through SPE cartridges (Oasis HLB, Waters, USA) preconditioned with 15
182 mL methanol and 10 mL Milli-Q water. The retained organic matter was subsequently
183 eluted with 10 mL methanol. The eluate was then concentrated to approximately 0.5
184 mL using a rotary evaporator and stored at -20 °C until analysis. Prior to analysis, the
185 sample was re-dissolved in 4 mL of methanol and filtered through a 0.22 µm PTFE
186 membrane. FR-ICR MS analysis was performed with a capillary voltage of 4.0 kV,
187 and samples were introduced into the ESI source at a flow rate of 120 µL/ h. Mass
188 spectra were acquired over the m/z range of 150 – 800 Da. To improve the
189 signal-to-noise ratio and dynamic range, each spectrum was averaged from 200 scans.

190 Blank samples were analyzed under the same procedure. Notably, no water-insoluble
191 precipitates larger than 0.22 μm were observed during photooxidation. However,
192 filtration of the reaction solution through a 0.22 μm membrane prior to analysis may
193 resulted in the loss of some newly formed oligomers.

194 The Composer software (Sierra Analytics, USA) was utilized to process the
195 FT-ICR MS spectra and assign elemental compositions to recalibrated peaks, with a
196 mass tolerance of ± 1.0 ppm and a signal-to-noise ratio (S/N) threshold of ≥ 4 . Based
197 on the assigned molecular formulas, WSOM compounds were categorized into four
198 groups: CHO, CHON, CHOS, and CHONS. To evaluate the degree of unsaturation
199 and aromaticity, double bond equivalent (DBE) and aromaticity index (AI) were
200 calculated as follows:

$$201 \quad \text{DBE} = \frac{1}{2} \times (2c + 2 - h + n) \quad (2)$$

$$202 \quad \text{AI} = \frac{1 + c - 0.5o - s - 0.5h}{c - 0.5o - s - n} \quad (3)$$

203 The intensity-weighted averaged characteristic parameters can be expressed as:

$$204 \quad P_w = (\sum P_i I_i) / \sum I_i \quad (4)$$

205 where P represents DBE, AI, molecular weight (MW), oxygen-to-carbon (O/C) or
206 hydrogen-to-carbon (H/C) ratio. P_i represents the corresponding parameter value for
207 each individual compound I , and I_i represents the relative abundance of its molecular
208 formula.

209 Molecular formulas were further classified into seven compound classes based
210 on their H/C and O/C ratios (Ning et al., 2025): lipid-like ($1.5 < \text{H/C} \leq 2.0$, $0 \leq \text{O/C} \leq 0.3$);
211 aliphatic -like ($1.5 < \text{H/C} \leq 2.2$, $0.3 < \text{O/C} \leq 0.67$); lignin-like ($0.67 < \text{H/C} \leq 1.5$, $0.1 \leq$

212 O/C < 0.67); carbohydrate-like (1.5 < H/C ≤ 2.5, 0.67 < O/C < 1.2); unsaturated
 213 hydrocarbon-like (0.67 < H/C ≤ 1.5, O/C < 0.1); unsaturated aromatic-like (0.2 ≤ H/C
 214 ≤ 0.67, O/C < 0.67), and tannin-(0.6 < H/C ≤ 1.5, 0.67 ≤ O/C ≤ 1.2). The saturated
 215 compounds were defined as the sum of lipid-like and aliphatic components.

216 2.6 High-resolution mass spectrometry analysis

217 High-resolution aerosol mass spectrometer (HR-AMS, Aerodyne Res. Inc.) was
 218 used to characterize the bulk chemical composition of aqSOA, including average
 219 elemental ratios (i.e., oxygen-to-carbon ratio (O/C) and hydrogen-to-carbon ratio
 220 (H/C)) and some specific fragment ions. The average oxidation state of carbon (OSc =
 221 2 × O/C – H/C) was used to index the oxidation degree of aqSOA. 10 mg/L ammonium
 222 sulfate was added into the solution as an internal standard for quantifying SOA mass
 223 concentration. The aqSOA mass yield was calculated as follows:

$$224 \text{aqSOA yield} = \frac{[Org]_t - [Org]_0}{[WSOC]_0 - [WSOC]_t} = \frac{[Org]_t \times \frac{[SO_4^{2-}]_t}{[SO_4^{2-}]_{AMS,t}} - [Org]_0 \times \frac{[SO_4^{2-}]_0}{[SO_4^{2-}]_{AMS,0}}}{([WSOC]_0 - [WSOC]_t) \times M/12} \quad (5)$$

227 Where $[SO_4^{2-}]_t$ and $[SO_4^{2-}]_0$ denote sulfate concentrations (mg/L) in the solution at
 228 irradiation time t and zero, respectively. Here, $[SO_4^{2-}]_t$ was equal to $[SO_4^{2-}]_0$ assuming
 229 sulfate was not loss during irradiation. The $[Org]$ and $[SO_4^{2-}]_{AMS}$ denote the apparent
 230 concentrations of aqSOA and sulfate measured by HR-AMS. $[WSOC]_t$ and $[WSOC]_0$
 231 were WSOC concentrations in the solution measured by TOC at irradiation time t and
 232 zero, respectively. M represents the averaged molecular weight of mixed solution
 233 which can be estimated by FT-ICR MS.

234 2.7 ROS determination based on electron paramagnetic resonance

235 Electron paramagnetic resonance (EPR) spectroscopy (Bruker EMXnano,
236 Germany) was used to detect ROS. 5,5-Dimethyl-1-pyrroline N-oxide (DMPO) and
237 2,2,6,6-tetramethylpiperidine (TEMP) were used as spin-trapping agents for α OH
238 and $^1\text{O}_2$ to identify the DMPO-OH adducts (1:2:2:1) and the TEMPO adducts (1:1:1),
239 respectively (Hu et al., 2025; Wang et al., 2020). The 10 mL of aqueous extracts were
240 diluted into 100 mL using deionized water and pH was adjusted at 5.0 ± 0.1 with 0.1
241 M H_2SO_4 solutions. Then 100 mM of two spin-trapping agents were added into the 50
242 mL of acidified aerosol extract solutions. After photodegradation of smoke extracts,
243 200 μL of solutions were transferred from the reaction solutions and immediately
244 analyzed by EPR. The EPR parameters were set as following: modulation frequency
245 of 100 kHz; center field of 3460 G, modulation amplitude of 1G, microwave power of
246 25 mW, sweep width of 200 G, sweep time of 150 s, number of scans of 20.

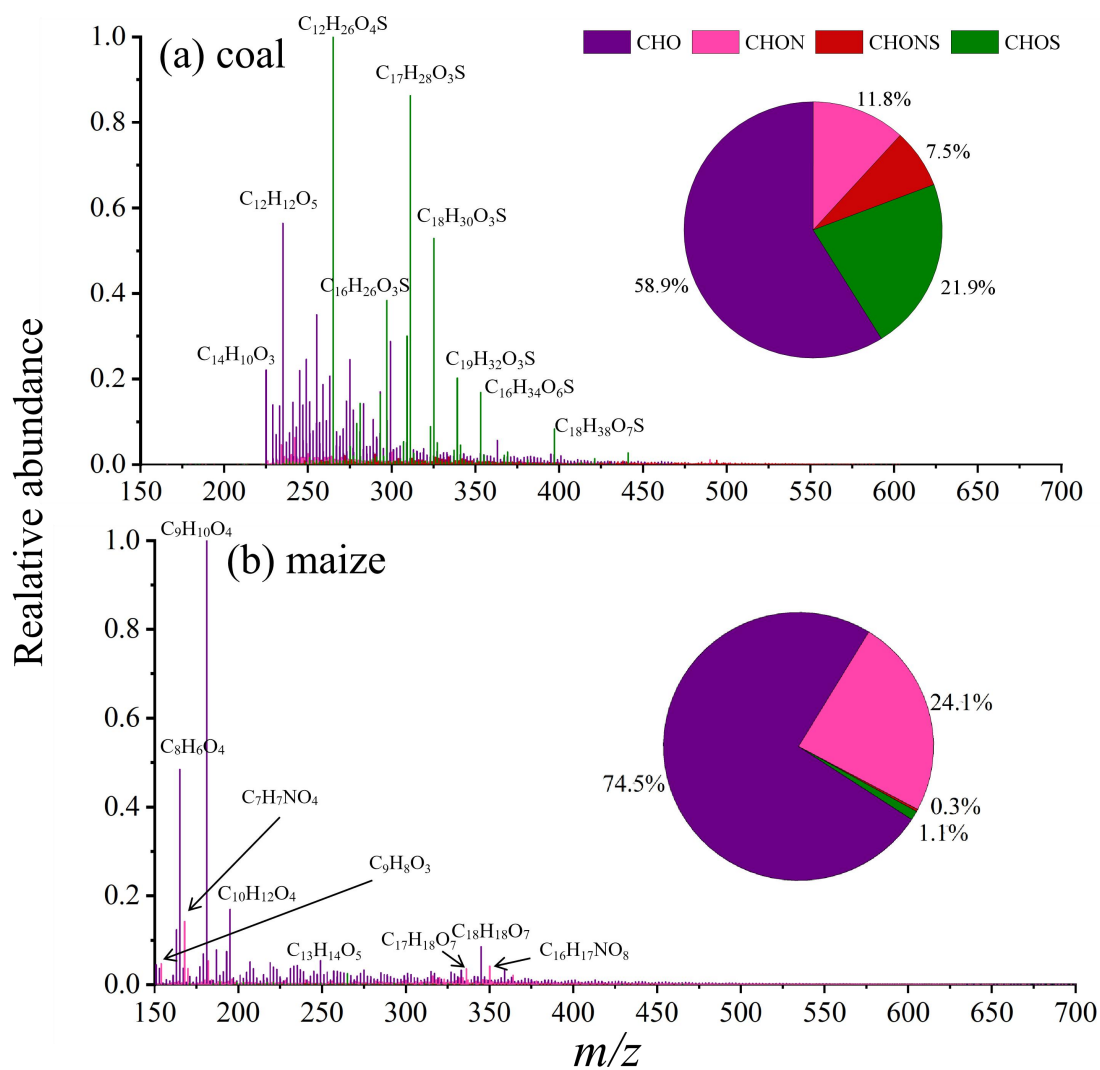
247 **3 Results and discussion**

248 **3.1 Comparison of fresh coal and maize smoke WSOM**

249 Fig. 1 showed the reconstructed FT-ICR mass spectra of WSOM for two fresh
250 extracts samples. Based on the intensity of each negative ion, the average molecular
251 formulas for coal and maize smoke extracts calculated as $\text{C}_{18.0}\text{H}_{24.0}\text{O}_{6.9}\text{N}_{0.90}\text{S}_{0.41}$ and
252 $\text{C}_{21.0}\text{H}_{21.7}\text{O}_{7.4}\text{N}_{0.86}\text{S}_{0.04}$, respectively, showing higher C in maize smoke extracts,
253 consistent with previous finding (Fan et al., 2016). In this study, these identified
254 molecular formulas were classified into four main compound groups based on their
255 compositions: CHO, CHON, CHOS, and CHONS. The relative abundances of the
256 four groups were determined by normalizing the magnitude of each peak to the total

257 magnitude of all identified peaks. Most peaks were located within the m/z range of
258 200–400. The greatest peak magnitudes were mainly distributed within the m/z range
259 of 250 -350. Distinct peak distribution patterns were observed for both smoke extracts.
260 For example, several CHOS compounds with high relative abundance, such as
261 $C_{12}H_{26}O_4S$, $C_{17}H_{28}O_3S$, $C_{18}H_{30}O_3S$, were identified in the coal smoke extract, whereas
262 the high-abundance CHO and CHON compounds, including $C_8H_{10}O_4$, $C_7H_7NO_4$, and
263 $C_{18}H_{18}O_7$ were predominant in the maize smoke extract. It should be noted that peak
264 magnitude is not indicative of a compound's concentration in a sample due to inherent
265 biases of C18 extractions and electrospray ionization efficiencies.

266 To better illustrate the differences in the \bullet OH oxidation behavior between the
267 two extracts, the concentrations of inorganic ions and transition metals (Fe and Cu) in
268 the fresh WSOM were also measured, as shown in Table S1. It can be seen that the
269 concentrations of Cl^- and NH_4^+ ions in maize were much higher than those in coal,
270 whereas the concentration of SO_4^{2-} ions in coal was higher than that in maize. During
271 the photochemical reaction, the concentrations of these ions showed little change. In
272 addition, the concentrations of Fe and Cu ions were very low, almost below the
273 detection limits of the instrument. These results indicate that the influence of ions on
274 the photochemical reaction can be neglected, especially that of Fe and Cu.



275

276 **Fig. 1.** Reconstructed ESI(-) FT-ICR mass spectra of (a) coal and (b) maize smoke extracts

277 colored by formula groups. The inserted pie charts show the percentage of four formula groups by

278 intensity.

279

280 3.2 Optical properties during photooxidation of smoke extracts

281 3.2.1 Absorbance characteristics

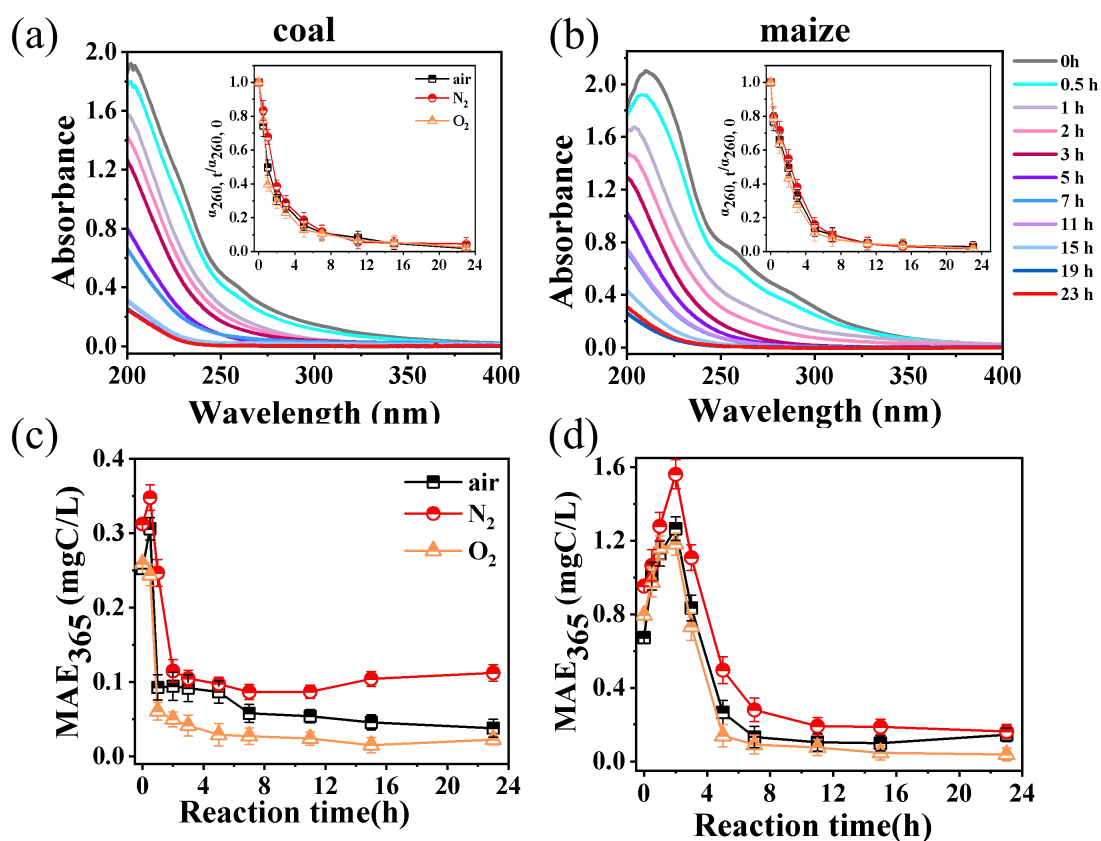
282 Aqueous $\bullet\text{OH}$ oxidation of two smoke extracts—involving both photolysis and

283 ROS oxidation reactions—can markedly alter their optical properties by degrading

284 existing chromophores or generating new light-absorbing compounds. Fig.2 (a, b)

285 shows the UV-vis absorbance spectra in the range of 200-500 nm of the reaction
286 solutions at varying irradiation time. Although the spectra were generally broad and
287 featureless, noticeable differences in the absorption intensity were observed between
288 coal and maize smoke. A distinct shoulder at 260 nm was observed in the spectra of
289 maize smoke WSOM, attributed to π - π^* transitions of unsaturated double bonds (e.g.,
290 C=C and C=O) (Li et al., 2021), indicating the presence of fulvic acid-like
291 chromophores. As the reaction progressed, overall decreases in absorbance (Fig. 2)
292 were observed for both smoke extracts, which can be ascribed to the degradation of
293 compounds containing carbonyl- and double bond groups. Tomaz et al. (2018)
294 similarly reported that aqueous α OH oxidation of complex BB mixtures led to rapid
295 depletion of phenolic compounds and formation of small organic acids. Consistent
296 with these findings, photobleaching (i.e. decrease in light absorbance) is the most
297 common effect observed upon irradiation of SOA or BrC in the aqueous phase (Jiang
298 et al., 2023). The decreased light absorption was likely due to competing processes,
299 including the formation of light-absorbing products and fragmentation yielding less
300 absorptive compounds. Study by Chen et al. (2025) on molecular structure-dependent
301 light absorption demonstrated that CHO compounds with low molecular weight and
302 high aromaticity are primarily responsible for absorption in the 200–300 nm range,
303 whereas CHON compounds (mainly nitroaromatics) and highly aliphatic structures
304 play a dominant role in absorption above 365 nm. However, the present results differ
305 from recent studies on aqueous SOA formation from the photooxidation of coal and
306 rice straw smoke WSOM, which reported photoenhancement at wavelength above

307 360 nm (Cao et al., 2025). Such discrepancies may be attributed to differences in light
 308 sources, \bullet OH concentrations, and the molecular composition of the smoke extracts.
 309 Clearly, different classes of compounds in smoke extracts exhibit distinct
 310 photochemical aging behavior, including photoenhancement, photobleaching or a
 311 combination of both.



312
 313 **Fig. 2.** (a, b) The UV-vis absorption spectra under different irradiation time for coal and maize
 314 smoke extracts, and (c, d) MAE at 365 nm over photoaging time. The inset shows the change in
 315 absorbance at the wavelength of 260 nm compared to the spectra at time zero.
 316
 317 Changes in MAC₃₆₅ are commonly used to track chromophore evolution since
 318 different chromophores exhibit varying light-absorbing ability. Fig. 2(c, d) shows the
 319 variation of the MAC₃₆₅ over reaction time for both smoke extracts. For both smoke

320 extracts, MAE₃₆₅ initially increased and then declined. The enhancement in
321 light-absorbing can be mainly ascribed to two factors (Jiang et al., 2021). First,
322 OH-addition to aromatic rings produces OH-rich compounds that act as chromophores
323 (Lei et al., 2024). Second, the formation of dimers and larger oligomers extends
324 π -conjugation, shifting absorption to longer wavelengths and enhancing light
325 absorption. Generally, increased functionalization and oligomerization increased light
326 absorption (Go et al., 2024; Vione et al., 2019). As the reaction proceeds, these
327 intermediate chromophores transform into smaller, ring-opened molecules with
328 weaker or negligible light absorption. The aqueous-phase photoaging of phenolic
329 SOA also showed that light-absorbing properties of oxidation products were strongly
330 time-dependent (Jiang et al., 2023). Additionally, photodegradation of WSOM can
331 generate more volatile products, and their evaporation may reduce WSOC (Fig. S1),
332 thereby influencing the light absorption per unit C mass. The final decrease in
333 MAE₃₆₅ can also be supported by the FT-ICR MS results (see Sect. 3.3). The observed
334 decrease in lignin-like fractions, together with reductions in DBE and AI values,
335 suggests the breakdown of these conjugated systems during aqueous photooxidation,
336 leading to a decline in MAE₃₆₅. Meanwhile, the formation of more saturated
337 compounds (e.g., lipid- and aliphatic-like species) further contributes to the decrease
338 in MAE₃₆₅. In addition, the formation of small oxygenated CHO species (e.g.,
339 carboxylic acids or CHO₂⁺ fragments from HR-AMS) with negligible absorbance at
340 365 nm dilutes the overall light-absorbing capacity. Another spectral parameter, E2/E3
341 (the ratio of absorbance at 250 nm to that at 365 nm), further characterizes these
342 changes. During the first hour of ω OH oxidation, E2/E3 decreased from 16 to 8 for
343 coal smoke, indicating enrichment in high-molecular-weight chromophores with
344 stronger light-absorbing capability. However, it increased from 12 to 22 for maize

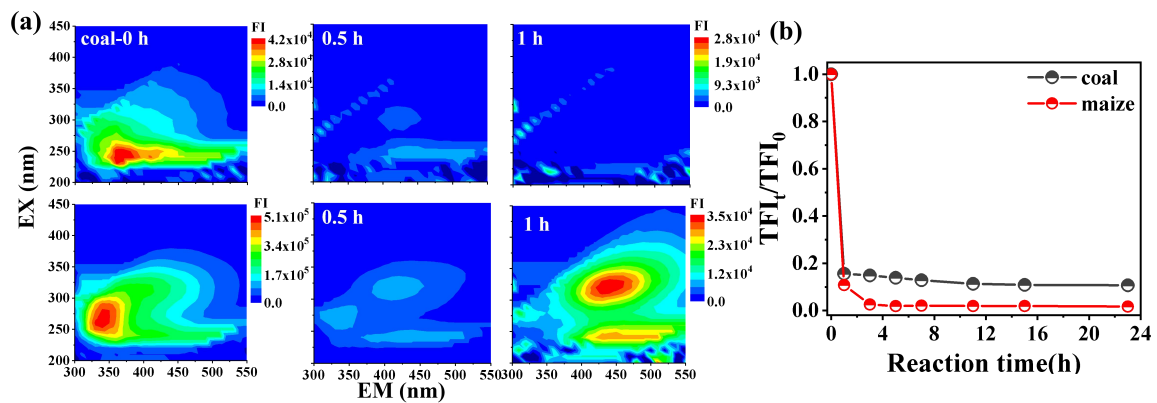
345 smoke extracts (Fig. S2). These contrasting E2/E3 trends highlight distinct molecular
346 transformations in WSOM for coal and maize smoke under α OH photooxidation.

347 **3.2.2 Fluorescence properties**

348 Fluorescence spectra provide more detailed molecular information than UV-vis
349 spectra. For example, a red shift in the excitation–emission maximum typically
350 indicates increased aromaticity and higher molecular weight (Tang et al., 2020). Fig.
351 3a presents the EEM spectra of both smoke samples upon irradiation. We observed a
352 rapid decrease in the characteristic fluorescence peak (Ex/Em = 275/350 nm) within
353 the first hour of the reaction. Concurrently, two new fluorescence peaks emerged at
354 Ex/Em = 325/400–500 nm and 225/400–500 nm, indicating the formation of
355 humic-like chromophores. As the reaction progressed, the intensities of these newly
356 formed peaks gradually declined. Consistently, HULIS-C concentrations increased
357 during the initial 1–3 h for both smoke extracts, followed by a gradual decrease over
358 time (Fig. S3). As shown in Fig. 3b, the total fluorescence intensity (Ex = 250–450
359 nm, Em = 300–650 nm) decreased sharply within the first hour and then declined at a
360 slower rate thereafter.

361 The HIX, BIX and FI were further employed to evaluate the degree of
362 humification and freshness of organic matters. As suggested by Wu et al. (2021), an
363 increased in HIX accompanied by decrease in BIX and FI can serve as indicators of
364 enhanced oxidation of atmospheric WSOC. As shown in Fig. S4, the HIX value
365 increased during the first hour and then decreased, suggesting that the formation of
366 humic-like substances initially exceeded their subsequent degradation. Conversely, FI

367 and BIX values decreased at the early stage of oxidation for both smoke samples (Fig.
 368 S4). In general, greater humification is associated with lower protein content,
 369 primarily due to a reduction in carbon-hydrogen compounds and a red shift in the
 370 fluorescence emission wavelength of more humified molecules. Conversely, a higher
 371 BIX indicates a higher contribution from protein-like and amino acid components.



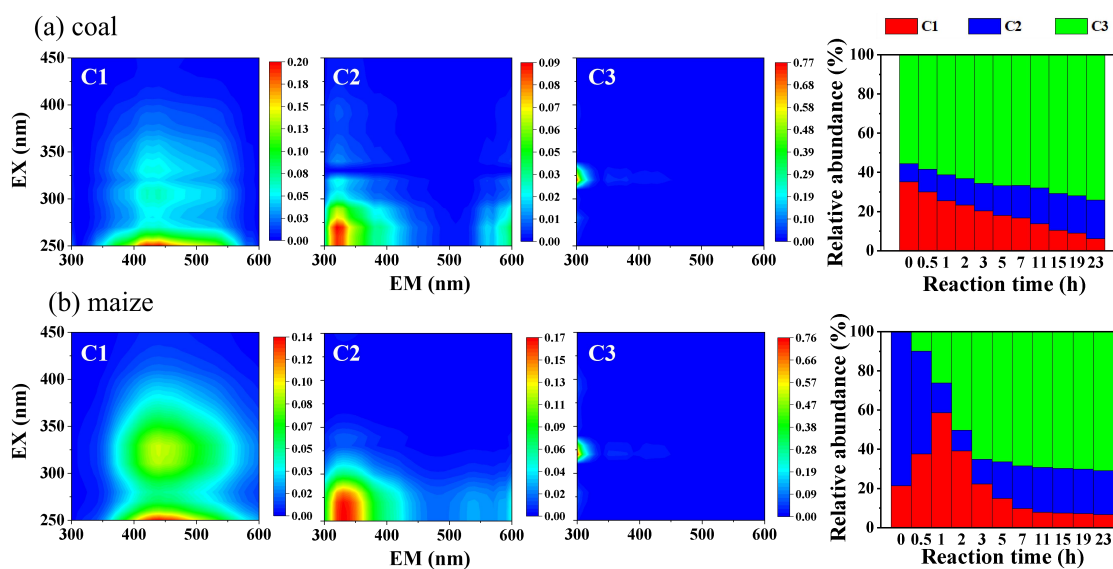
372
 373 **Fig. 3.** (a) Variation trend of EEM fluorescence spectra and (b) temporal profiles of total
 374 fluorescence intensity for two smoke extracts.

375

376 The PARAFAC model identified three underlying fluorescent components,
 377 including one humic-like components (C1) and two protein-like component (C2 and
 378 C3) (Fig. 3). Component C1 is considered to be a humic-related substance,
 379 characterized by two peaks at Ex/ Em=230/400–500 nm and 300/400-500 nm (Huang
 380 et al., 2025). C2 displays peaks at Ex/Em=250-300/300-350 nm, which can be
 381 attributed to tyrosine-like components. C3 (Ex/Em=325/300 nm) is likely link to
 382 tryptophan-like components. As shown in Fig. 4, the proportion of C1-C3 in both
 383 maize and coal WSOM varied dynamically throughout photochemical processes. For
 384 coal WSOM, C1 fraction decreased, whereas C2 and C3 increased. In contrast, for

385 maize WSOM, C2 gradually transformed into C1 at the first hour, resulting in
 386 opposite trends between the two components. This transformation likely reflects the
 387 formation of more oxygenated humic-like substances via OH-functionalization at the
 388 early stage, consistent with change trends of Hulis-C for maize smoke extracts (Fig.
 389 S3). This interpretation can be further confirmed by the increase in HIX values for
 390 maize smoke during the first hour of photooxidation (Fig. S4 c).

391 For both smoke WSOM samples, the C3 component exhibited a gradual increase
 392 over time. The findings are in accordance with other's study on the photooxidation of
 393 WSOC emitted from rice straw combustion (Zhang et al., 2021). The stronger
 394 fluorescence intensity observed at Ex/Em=325/300 nm may correspond to low-ring
 395 PAHs and their derivatives, which are known to be produced in abundance during
 396 biomass pyrolysis or burning (Mahamuni et al., 2020). Overall, the EEM components
 397 varied depending on the types of smoke-derived WSOM.



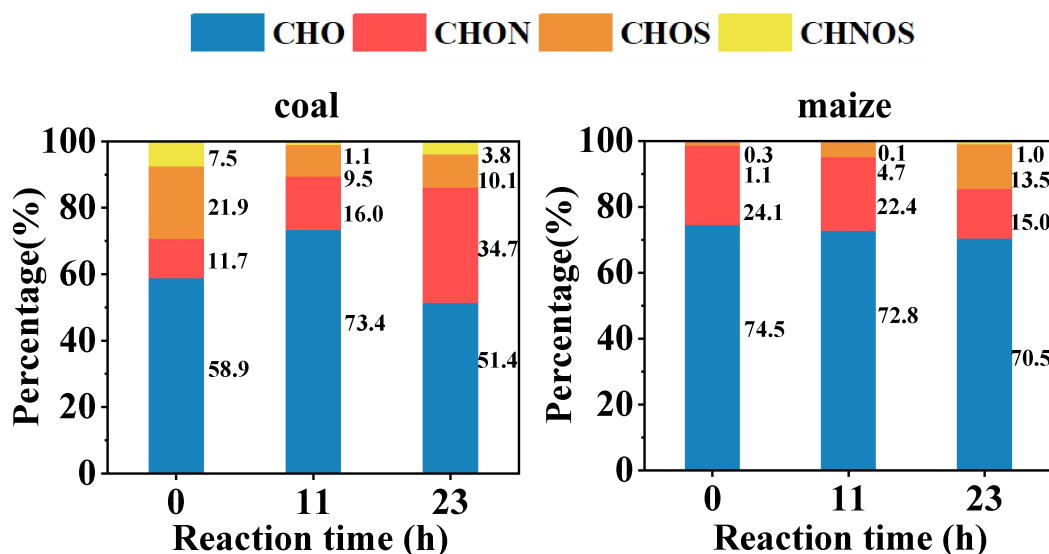
398
 399 **Fig. 4.** Three fluorescent components (C1-C3) of the smoke extracts identified by the
 400 EEM-PARAFAC model and variations in the relative contributions of each PARAFAC
 401 component of (a) coal and (b) maize smoke extracts with photoaging time.

402

403 3.3 Molecular composition of WSOM via FT-ICR MS

404 The intensity weighted average values of various molecular
405 parameters—including molecular weight (MW), elemental ratios (H/C and O/C), DBE,
406 AI—for maize and coal smoke extracts before and after photoaging were summarized
407 in Table 1. As listed in Table 1, a total number of 5596 and 5107 molecular formulas
408 were identified for fresh coal and maize extracts, respectively, within the m/z range of
409 100-600, indicating the complicated molecular compositions of WSOM. For coal
410 WSOM, the MW decreased slightly 313 g/mol in the fresh sample to 296 and 288
411 after 11 h and 23 h photooxidation, respectively. The MW for maize remained nearly
412 unchanged during OH-photooxidation. The dominant species in both smoke extracts
413 were CHO and CHON compounds, with higher abundance observed in maize than in
414 coal smoke extract (Fig. 5). Molecular composition analysis further revealed that
415 maize smoke WSOM was largely composed of CHO and CHON, together accounting
416 for 98.6% of the total peak area. CHO compounds constituted more than half of all
417 identified molecular formulas in both WSOM samples (74.5% for maize and 58.9%
418 for coal). In contrast, S-containing compounds (CHOS and CHONS) were much more
419 abundant in coal smoke extracts (29.4% in total) than in maize (1.4% in total).
420 Similarly, previous studies reported that the fractions of S-containing CHOS and
421 CHONS species in crop-derived WSOM were relatively low (3-9% in peak area) (Li
422 et al., 2024). Interestingly, S-containing compounds in coal smoke decreased by
423 nearly 50% after photodegradation, whereas their abundance increased markedly in
424 maize smoke extracts. Meanwhile, the proportion of CHON compounds in coal
425 smoke increased under photoaging, which may be attributed to the photochemical
426 transformation of CHONS species and/or the oxidation of reduced CHN compounds.
427 Conversely, the CHON proportion in maize smoke decreases with reaction time,

428 likely due to the progressive degradation of nitroaromatic compounds commonly
 429 present in biomass burning emissions (Lin et al., 2016).



430
 431 **Fig. 5.** Change of relative abundance fraction of four groups (CHO, CHON, CHOS, and CHONS)
 432 with reaction time in both smoke extracts.

433 The molecular-level parameters are summarized in Table 1. DBE values ranged
 434 from 2 to 9 for coal-smoke WSOM and from 2 to 11 for maize-smoke WSOM. The
 435 degree of unsaturation and aromaticity of molecular formulas can be valuated using
 436 the H/C ratio and DBE values, with lower H/C ratios and higher DBE indicating
 437 greater unsaturation and, to some extent, stronger aromatic character. As shown in
 438 Table 1, after 23 h of photooxidation, aged WSOM exhibited higher H/C ratios (1.75
 439 vs. 1.32 for coal; 1.68 vs. 1.02 for maize), lower DBE values (3.85 vs. 7.12 for coal;
 440 4.08 vs. 8.99 for maize), and reduced AI values (0.16 vs. 0.31 for coal; 0.16 vs. 0.48
 441 for maize) compared to the fresh samples. These concurrent changes consistently
 442 indicate the breakdown of aromatic structures and an overall shift toward more
 443 saturated compounds. This trend agrees with previous findings from dark aqueous •

444 OH oxidation of BB smoke WSOC reported by Fan et al. (2024).

445 At the molecular-class level, CHON compounds in maize smoke initially exhibit a
446 relatively high average molecular weight (MW, 329.45 g/mol) and DBE (10.52).
447 Upon photolysis, the average MW decreases to 301.07 g/mol (11 h) and 296.44 g/mol
448 (23 h), while the DBE declines to 6.59 and 4.14, respectively. These changes reflect
449 the progressive breakdown of conjugated structures and a corresponding reduction in
450 aromaticity, consistent with the observed decrease in light absorbance (Fig.2 b). For
451 coal smoke, a considerable fraction of CHONS species undergoes transformation into
452 CHON compounds with lower aromaticity and DBE during photolysis. This
453 conversion increases the relative abundance of CHON species while contributing to a
454 decrease in overall molecular weight. In addition, the MW of CHO compounds in
455 coal smoke decreases progressively with photolysis. In contrast, maize-smoke WSOM
456 is dominated by CHO compounds, whose MW remains relatively unchanged during
457 photolysis, resulting in only minor variation in the bulk molecular weight. This
458 contrast primarily reflects differences in the initial WSOC compositions between coal
459 and maize smoke. Overall, the marked decreases in AI and DBE for CHON
460 compounds in both smokes indicate substantial loss of aromaticity, which in turn
461 contributes to the reduction in light absorption.

462 Additionally, the O/C increased from 0.38 to 0.45 for coal and from 0.40 to 0.55
463 after 11 h of oxidation, followed by a decrease to 0.27 and 0.25 at 23 h, respectively.
464 This trend indicates a transformation from OH-functionalization to fragmentation as
465 photooxidation progressed. A decrease in DBE per carbon (DBE/C) was observed
466 after 23 h of photodegradation—from 0.45 to 0.25 for coal and 0.62 to 0.27 for

467 maize—further confirming the transformation of refractory aromatic-condensed
 468 structures into more polar and readily degradable small molecules. Fig. S5 shows the
 469 relationship between DBE values and C atom numbers for four compound groups
 470 identified by FT-ICR MS.

471 **Table 1** Intensity-weighted average molecular parameters (MW, elemental ratios, DBE, DBE/C,
 472 AI) of coal and maize smoke WSOM before and after $\cdot\text{OH}$ photooxidation

| Sample | Time | Elemental composition | Formulas number | MW (g/mol) | DBE | AI | O/C | H/C | DBE/C |
|--------|------|-----------------------|-----------------|------------|------|------|------|------|-------|
| coal | 0 h | Total | 5596 | 312.98 | 7.12 | 0.31 | 0.38 | 1.32 | 0.45 |
| | | CHO | 1728 | 300.23 | 8.16 | 0.38 | 0.36 | 1.16 | 0.52 |
| | | CHON | 1695 | 323.12 | 8.77 | 0.43 | 0.49 | 1.25 | 0.54 |
| | | CHOS | 702 | 310.03 | 3.60 | 0.10 | 0.31 | 1.74 | 0.23 |
| | | CHONS | 1471 | 406.27 | 6.61 | 0.19 | 0.55 | 1.48 | 0.41 |
| | 11 h | Total | 5157 | 296.35 | 4.58 | 0.17 | 0.45 | 1.57 | 0.34 |
| | | CHO | 2066 | 286.35 | 4.61 | 0.16 | 0.47 | 1.54 | 0.35 |
| | | CHON | 2029 | 312.31 | 4.10 | 0.16 | 0.40 | 1.68 | 0.31 |
| | | CHOS | 816 | 343.04 | 4.93 | 0.16 | 0.29 | 1.62 | 0.29 |
| | | CHONS | 246 | 329.73 | 6.45 | 1.01 | 0.86 | 1.63 | 0.54 |
| | 23 h | Total | 5072 | 288.32 | 3.85 | 0.16 | 0.27 | 1.75 | 0.25 |
| | | CHO | 1348 | 262.69 | 4.04 | 0.15 | 0.26 | 1.66 | 0.28 |
| | | CHON | 1970 | 304.36 | 2.03 | 0.07 | 0.25 | 1.99 | 0.14 |
| | | CHOS | 723 | 313.19 | 4.80 | 0.17 | 0.31 | 1.67 | 0.27 |
| | | CHONS | 1031 | 398.63 | 7.04 | 0.33 | 0.52 | 1.63 | 0.39 |

| | | | | | | | | | |
|-------|------|-------|------|--------|-------|------|------|------|------|
| | | Total | 5107 | 286.90 | 8.99 | 0.48 | 0.40 | 1.02 | 0.62 |
| | | CHO | 2143 | 273.62 | 8.56 | 0.46 | 0.40 | 1.02 | 0.61 |
| | 0 h | CHON | 2772 | 329.45 | 10.52 | 0.54 | 0.40 | 0.98 | 0.66 |
| | | CHOS | 107 | 248.21 | 4.61 | 0.22 | 0.46 | 1.37 | 0.47 |
| | | CHONS | 85 | 317.32 | 7.31 | 0.28 | 0.56 | 1.13 | 0.61 |
| | | Total | 6027 | 288.84 | 5.44 | 0.21 | 0.55 | 1.40 | 0.44 |
| | | CHO | 2643 | 283.95 | 5.19 | 0.19 | 0.56 | 1.41 | 0.42 |
| maize | 11 h | CHON | 2954 | 301.07 | 6.59 | 0.30 | 0.57 | 1.29 | 0.54 |
| | | CHOS | 395 | 305.41 | 3.69 | 0.12 | 0.35 | 1.83 | 0.20 |
| | | CHONS | 35 | 317.42 | 10.37 | 0.45 | 0.23 | 1.19 | 0.54 |
| | | Total | 5147 | 285.81 | 4.08 | 0.16 | 0.25 | 1.68 | 0.27 |
| | | CHO | 2647 | 277.01 | 4.20 | 0.16 | 0.23 | 1.65 | 0.27 |
| | 23 h | CHON | 1995 | 296.44 | 4.14 | 0.19 | 0.28 | 1.69 | 0.30 |
| | | CHOS | 400 | 312.24 | 2.94 | 0.09 | 0.34 | 1.86 | 0.18 |
| | | CHONS | 105 | 393.70 | 10.63 | 1.03 | 0.49 | 1.11 | 0.67 |

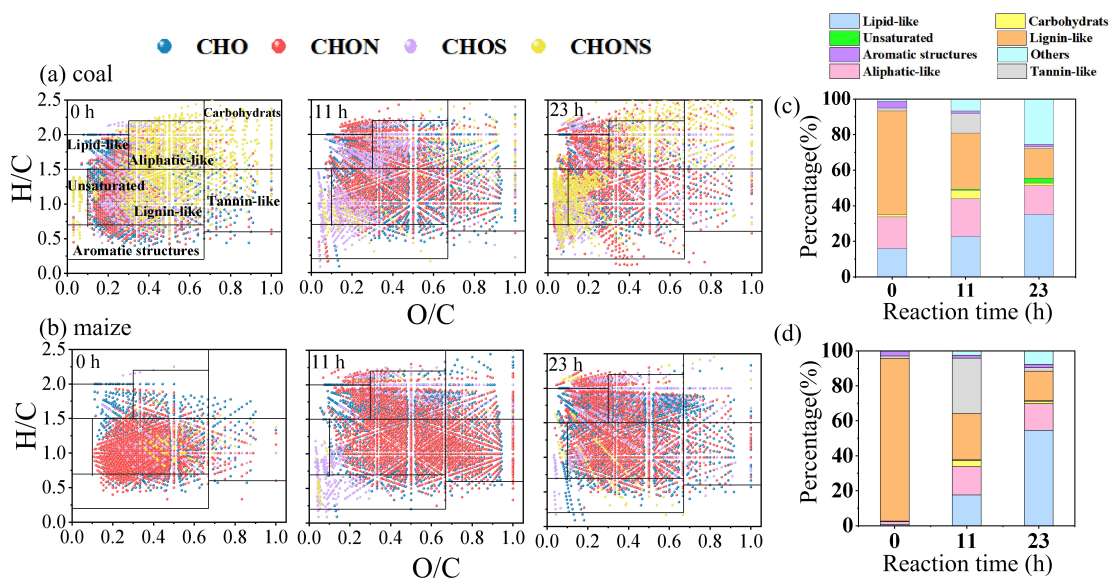
473

474 The van Krevelen diagram (Fig. 6), which plots the O/C ratio as the x-axis and
475 the H/C ratio on the y-axis, was used to elucidate the molecular distribution. For
476 clarity, the corresponding detailed values were listed in Table S2. Lignin-like
477 compounds dominated both coal and maize smoke WSOM, accounting for 58.2% and
478 93.1% of total intensity, respectively, indicating a greater abundance of phenolic
479 organic species in maize smoke. Previous study also showed that CHO formulas were
480 mainly lignin-pyrolysis products (Song et al., 2018). After photoaging, the lignin-like

481 fraction decreased significantly, reflecting the degradation of aromatic phenolic
482 species. Given that most lignin-like compounds possess strong light-absorbing
483 properties, their decomposition directly contributed to the observed decrease in
484 absorbance. In contrast, the intensity of saturated compounds (sum of lipids and
485 aliphatic components) increased substantially after OH-induced photooxidation, from
486 33.8 % to 51.2% at 23 h for coal and from 2.4% to 69.8 % for maize. These
487 observations suggest a significant increase in saturated aliphatic and O-enriched
488 compounds after •OH photooxidation.

489 As listed in Table S2, the initial increase followed by a decrease (from 11.2% to
490 1.1% for coal and 31.8% to 2.1% for maize smoke) in tannin-like compounds
491 suggests that radical coupling, condensation, or addition reactions likely occurred
492 during the early stage of the reaction, leading to a higher O/C ratio at 11 h compared
493 to the fresh sample.

494 Condensed aromatic molecules, characterized by low H/C and O/C ratios but
495 high AI, showed a slight decrease with photoaging, indicating the partial degradation
496 of highly aromatic structures. Overall, the reduction in aromatic and lignin-like
497 compounds aligns with the observed decline in the light-absorbing properties (see
498 Sect. 3.2.1). In all, aromatic and lignin-like compounds were continuously
499 transformed into lipid- and aliphatic-like compounds. During the initial stage (first 5
500 h), carbohydrate-like substance such as oxalate were generated (Fig. S6), but their
501 abundance subsequently decreased, consistent with the pH variation that first declined
502 (initial 3 h) and then increased again (Fig. S7). The formation of carboxylic acids can
503 be further confirmed later by identifying their characteristic fragment ions using



505

506 **Fig. 6.** (a, b) Van Krevelen diagrams of four groups (CHO, CHNO, CHOS, and CHNOS) and (c, d)

507 Intensity-weighted fractions of seven major molecular classes. Saturated compounds represent the

508 sum of lipid-like and aliphatic components. Unsaturated represents unsaturated hydrocarbons.

509

510 To further elucidate the photooxidation behaviors of both smoke extracts, the

511 number proportions of resistant, degraded and newly produced molecules were

512 summarized in Table S3. After 11 h of irradiation, 55.1 % and 58.2% of the total

513 formulas in fresh coal and maize, were degraded, resulting in 51.3% and 64.6% newly

514 formed formulas. From 11 h to 23 h, the numbers of newly produced and degraded

515 molecules increased slightly for coal but decreased for maize. Fig. 7 illustrates the

516 O/C vs. H/C distributions of degraded and newly formed compounds after 11 h and 23

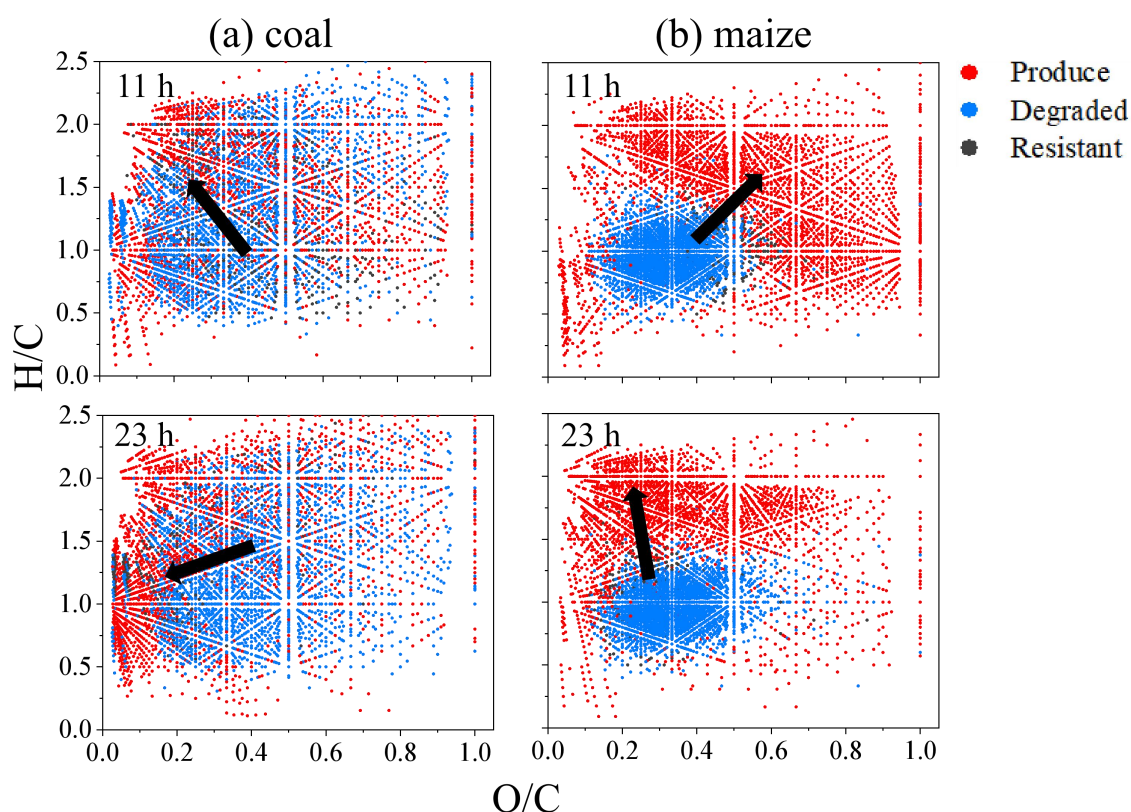
517 h of photodegradation. For coal, most degraded compounds were located in high O/C

518 regions, whereas some newly formed species with much lower O/C and higher H/C

519 were likely associated with unsaturated hydrocarbons and lipid-like species. In

520 contrast, maize exhibited a marked shift from low to high O/C and H/C compounds at
521 11 h, resulting in an increase in average O/C ratio. This trend suggests that maize
522 compounds mainly underwent functionalization during the first stage—introducing
523 oxygen-containing groups without breaking the carbon skeleton, thereby increasing
524 O/C and slightly lowering or maintaining H/C. The shift toward higher O/C ratios in
525 the van Krevelen diagram further supports the progression from aromatic to more
526 oxygenated and saturated compounds for maize smoke WSOM.

527 Overall, these results reveal distinct degradation pathways and product
528 characteristics for coal and maize smoke extracts.



529

530 **Fig. 7.** Van Krevelen diagrams of resistant, degraded and produced formulas in WSOM derived

531 from (a) coal and (b) maize burning before and after OH photooxidation.

532 **3.4 AqSOA composition and mass yield**

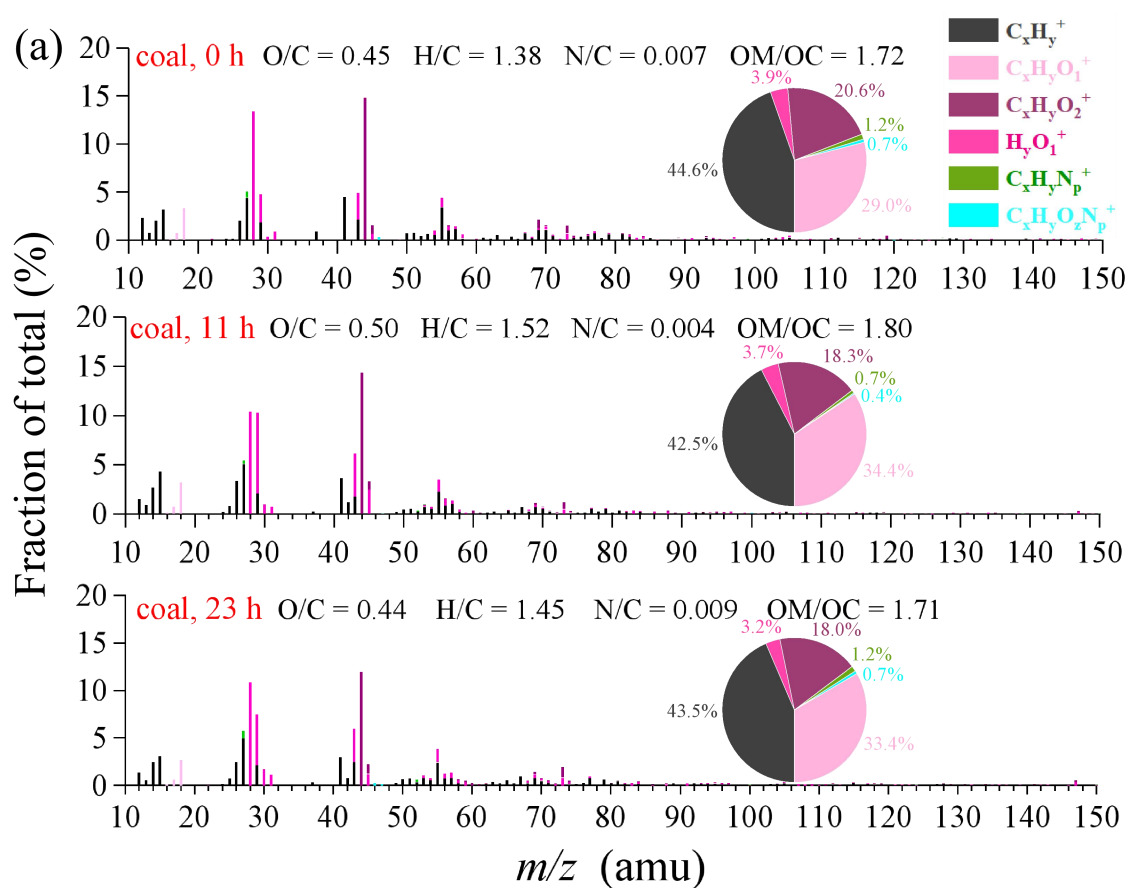
533 The aqSOA spectra exhibited higher mass fractions of $C_xH_y^+$ and $C_xH_yO_1^+$
534 ions but lower fractions of $C_xH_yN_p^+$ and $C_xH_yO_xN_p^+$ ions (Fig. 8). For corn-derived
535 aqSOA, the fractions of $C_xH_y^+$ and $C_xH_yO_1^+$ both decreased by approximately 10%
536 with increasing photolysis time, while $C_xH_yO_2^+$ increased substantially from 15.95%
537 to 29.96% after 23 h of photoreaction. In contrast, for coal-derived aqSOA, the
538 fraction of $C_xH_yO_1^+$ increased with irradiation time, while no corresponding increase
539 in $C_xH_yO_2^+$ was observed. This suggests that the overall oxidation degree of
540 coal-derived aqSOA did not increase significantly relative to that prior to irradiation.

541 Table S4 summarizes the chemical properties, mass concentration and yield of
542 the formed aqSOA and their evolution during the photoreaction. During the first 5 -7
543 h, both f_{44} and OSc values increased, indicating a progressive enhancement in the
544 oxidation state of aqSOA for both samples. In contrast, the H/C ratio exhibited only
545 minor changes throughout the reaction, suggesting relatively stable bulk hydrogen
546 content despite ongoing oxidation. A comparison between the two systems further
547 reveals that maize-derived aqSOA undergoes a more pronounced increase in
548 oxidation at the early stage, likely driven by functionalization reactions. As
549 photochemical processing continues, however, a slight decline in oxidation is
550 observed, which can be attributed to fragmentation processes. This trend is less
551 evident in coal-derived aqSOA, highlighting differences in their underlying
552 transformation mechanisms. Notably, the significantly higher O/C ratios and OSc of
553 maize-derived aqSOA compared to those of the precursors suggest that aqueous-phase
554 processing can serve as an effective source of oxygenated SOA in regions influenced
555 by biomass burning emissions. The value of f_{43} remained relatively low value (less
556 than 0.1) and is therefore not discussed further.

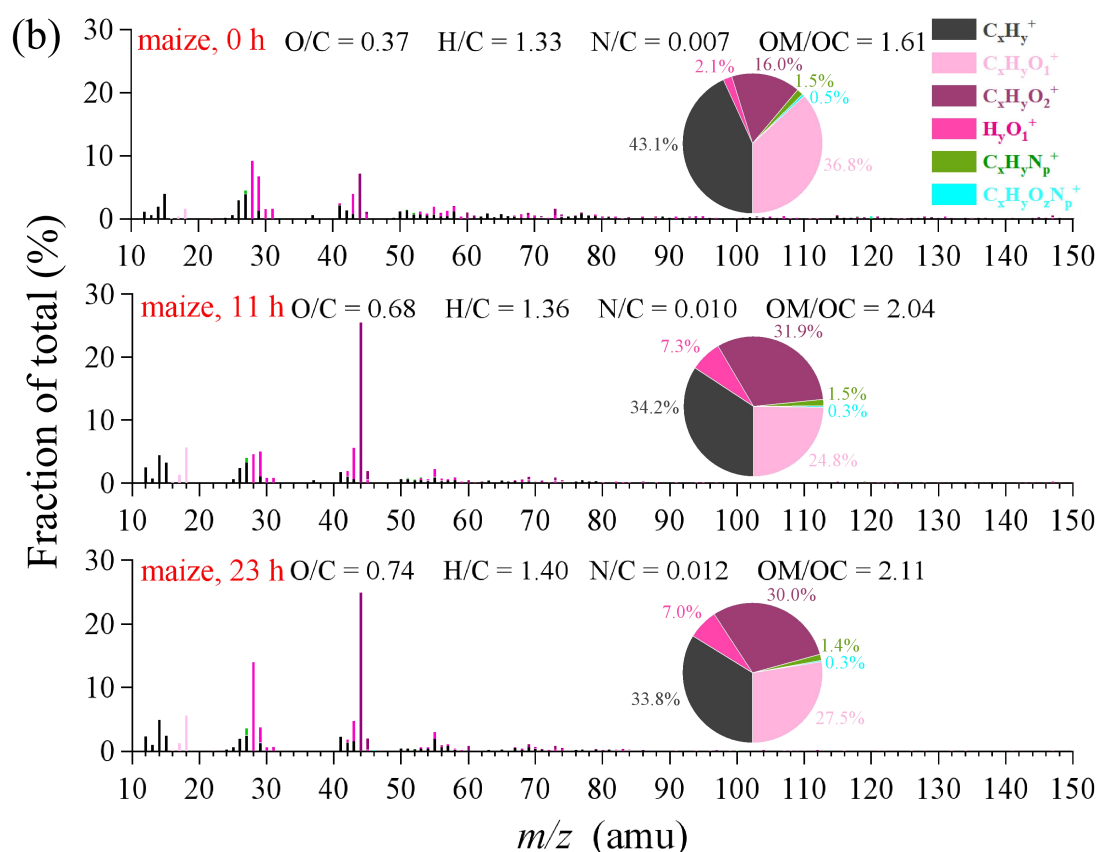
557 For coal samples, the aqSOA mass concentration ranged from 50.77 mg/L to
558 126.95 mg/L. It reached a minimum at 11 h and subsequently increased to 126.95
559 mg/L at 23 h. Correspondingly, the aqSOA mass yield peaked at 148.44% at 1 h,
560 continuously decreased to 1.87% within 9 h, and then increased again to 33.91% at 23
561 h. The aqSOA mass yield of maize was significantly lower (less than 10%) than that
562 of coal samples, indicating that coal sample is more efficient at generating
563 low-volatility species compared to maize. The possible reasons why coal-derived
564 aqSOA is higher than that from maize are as follows. First, the fresh coal-derived
565 CHOS compounds are dominated by species such as $C_{17}H_{28}O_3S$ and $C_{18}H_{30}O_3S$,
566 which are mainly organosulfates. These compounds have relatively high saturation
567 and stability, and undergo little change upon photolysis, resulting in a high SOA mass
568 yield measured by HR-AMS. In contrast, maize-derived WSOM is primarily
569 composed of lignin-like substances with high DBE values, which are more susceptible
570 to OH functionalization, forming saturated fatty acids or polyhydroxy acids (e.g.,
571 $C_9H_{18}O_6$ and $C_9H_{10}O_7$). These products can further undergo fragmentation into
572 smaller, more volatile products (e.g., low-molecular-weight acids), leading to a lower
573 aqSOA mass yield.

574 The significant formation of carboxylic acids during the first 9 h of photoreaction
575 is further evidenced by the Van Krevelen diagram (H/C versus O/C), in which aqSOA
576 evolves along a slope of approximately -1 throughout the photooxidation process (Fig.
577 S8). Consistently, the CHO_2^+ ion in the aqSOA AMS spectra—commonly used as a
578 tracer for carboxylic functional groups—exhibits a continuous increase during the
579 first 5 h of photoreaction (Fig. S9). After 3–9 h of reaction, the concentration of
580 CHO_2^+ decreases, accompanied by a decline in f_{44} . A plausible explanation is the

581 occurrence of fragmentation reactions, during which the oxidation products initially
 582 formed through oligomerization or functionalization decompose into smaller, more
 583 oxidized species. This trend has also been reported in previous studies on the
 584 photooxidation of phenolic carbonyls (Jiang et al., 2021).



585



586

587 **Fig. 8.** High-resolution MS profiles for aqSOA products at 0 h, 11 h and 23 h for (a) coal and (b)
 588 maize. The peaks in the mass spectra are color-coded according to six ion categories: $C_xH_y^+$,
 589 $C_xH_yO_1^+$, $C_xH_yO_2^+$, $H_yO_1^+$, $C_xH_yN_p^+$ and $C_xH_yO_xN_p^+$ ions. The inserted pie charts denote the mass
 590 fraction of each ion family to the total MS.

591

592 3.5 DTT analysis

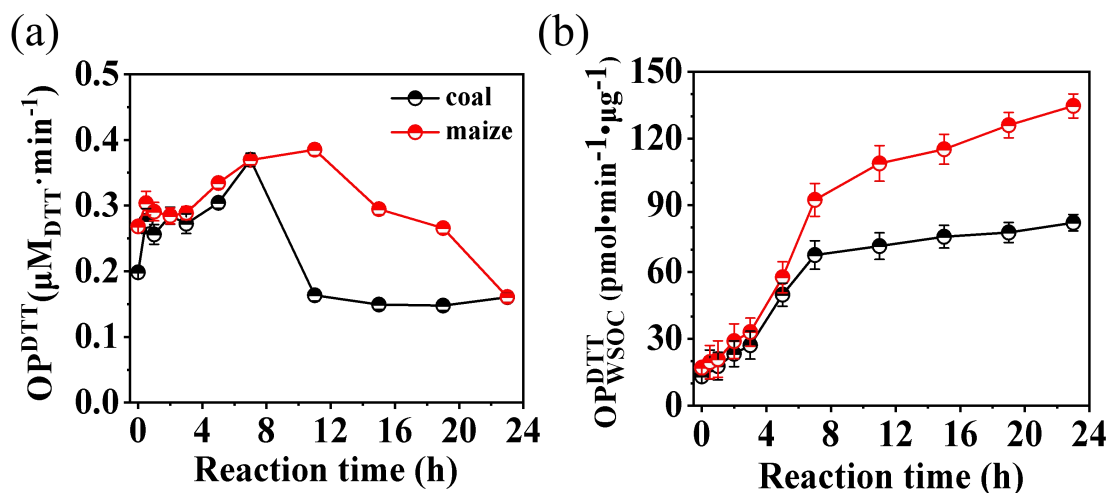
593 Aqueous photochemical aging of BB smoke can also alter its toxicity. The
 594 oxidative potential of the reaction solutions was evaluated using the dithiothreitol
 595 (DTT) assay, as described in our previous work (Ye et al., 2025). As shown in Fig. 9a,
 596 based on the DTT consumption rate (OP^{DTT}), OH-initiated photooxidation of smoke
 597 extracts led to an increase in OP^{DTT} during the first 1 h. Upon prolonged photoaging,
 598 the OP^{DTT} value decreased to $0.15 \mu\text{M DTT min}^{-1}$ after 23 h, slightly lower than the
 599 corresponding initial values. Previous research results also suggested that aqueous OH
 600 oxidation of WS-BBOA components generally leads to a final reduction in OP^{DTT}
 601 (Wong et al., 2019; Jiang and Jang, 2018) during prolong irradiation, consistent to our
 602 findings. The temporal variation pattern of OP^{DTT} is comparable to that observed for

603 aqueous oxidation of soybean straw extracts (Ye et al., 2025), but opposite to that of
604 4NC photodegradation (Lei et al., 2025). The DTT activity is likely associated with
605 light-absorbing and fluorescent substances containing large conjugated electron
606 systems, which can transfer electrons to participate in catalytic reaction, thereby
607 contributing to DTT activity (Chen et al., 2019). The reduction in DTT activity after
608 23 h agrees with the decrease of lignin-like and aromatic compounds revealed by
609 FT-ICR MS analysis.

610 Given that aqueous OH oxidation did not significantly reduce the total WSOC
611 concentrations, the decrease in OP^{DTT} is likely attributed to the formation of non- or
612 less DTT-active components. However, total WSOC decreased significantly upon
613 aging; consequently, the OP^{DTT} normalized by WSOC increased over irradiation time,
614 suggesting the possible formation of secondary toxic organic species during the aging
615 processes. Previous published studies have also showed that photochemical aging of
616 fresh particles can either enhance or diminish toxicity, depending on their sources and
617 oxidation conditions (Fang et al., 2024). To further characterize the ROS-generation
618 potential of WSOM from different combustion sources, we calculated the
619 WSOC-normalized DTT consumption rate (OP_{WSOC}^{DTT} , OP^{DTT} divided by WSOC). The
620 results showed that the mass-normalized DTT consumption rates gradually increased
621 and reached a plateau at 132 and 82 pmol/min/ μ g for maize and coal smoke extracts,
622 respectively, similar to finding from Wong et al. (2019). These values are higher than
623 those reported for water extracts from PM_{2.5} aerosol (22-68 pmol·min⁻¹· μ g⁻¹) (Verma et
624 al., 2012). Based on the molecular-level differences after •OH photooxidation, the
625 reasons for the OP_{WSOC}^{DTT} changes induced by OH-photolysis in coal and maize are
626 likely different. For coal, the increase in OP_{WSOC}^{DTT} may primarily result from the
627 formation of CHON compounds after photolysis, whereas for maize, the increase is

628 probably due to the production of more quinone species or OH addition products
629 during the reaction (Tang et al., 2025; Wong et al., 2019).

630 Unfortunately, due to the limitations of current analytical techniques, it remains
631 challenging or even impossible to attribute the observed DTT variation trends to
632 specific molecular species.



633
634 **Fig. 9.** (a) Temporal evolution of DTT consumption rate and (b) WSOC-normalized DTT activity
635 for both smoke extracts during aqueous OH photooxidation.

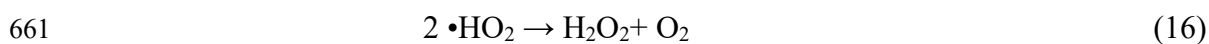
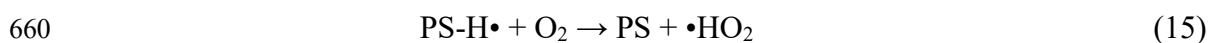
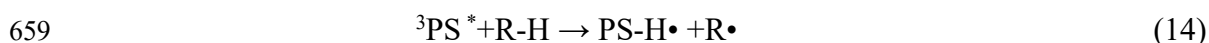
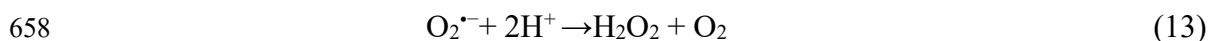
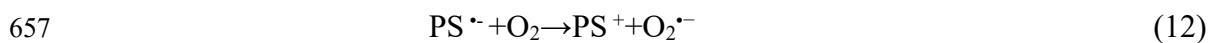
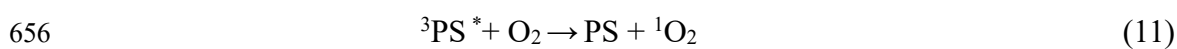
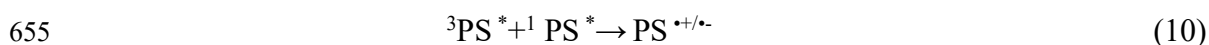
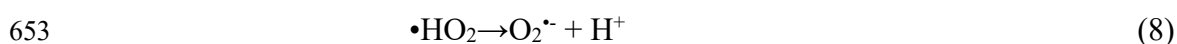
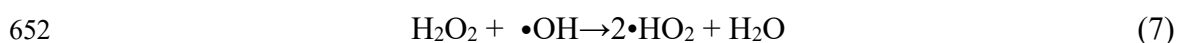
636 3.6 ROS contribution and reaction mechanism

637 3.6.1 ROS concentration and relative contribution

638 Hydrogen peroxide can undergo photolysis to generate $\bullet OH$, which effectively
639 break down chromophores, thereby decreasing light absorption. The OH radicals can
640 oxidize most organic species, leading to a sharp decrease in both WSOC and
641 absorbance during the initial reaction stage.

642 According to previous studies (Arciva et al., 2022), when the concentration of the
643 BB mixture reaches 12 mg C/L, the concentration of photosensitizers in solution can
644 exceed several millimoles. This suggests that the smoke samples in the present study

645 likely contains substantial amounts of photosensitizing compounds. Upon exposure to
 646 sunlight, these photosensitizer (denoted as PS) absorb photons and transition to their
 647 triplet excited state ($^3\text{PS}^*$). The excited triplet states can subsequently react with O_2 to
 648 produce various ROS, including $^1\text{O}_2$, superoxide ($\text{O}_2^{\cdot-}$), hydroperoxyl radical (HO_2^{\cdot}),
 649 and OH^{\cdot} , through H-abstracting, electron transfer and energy transfer processes.
 650 These ROS species actively participate in subsequent photooxidation reactions.



662 According to method described in Section 2.7, the steady-state concentrations of $\cdot\text{OH}$
 663 (denoted as $[\cdot\text{OH}]_{\text{ss}}$) and $^1\text{O}_2$ (denoted as $[^1\text{O}_2]_{\text{ss}}$) were determined using EPR. The
 664 distinct 1:1:1 triplet EPR signal characteristic of $^1\text{O}_2$ and 1:2:2:1 quartet signal of $\cdot\text{OH}$
 665 confirmed the generation of $^1\text{O}_2$ and $\cdot\text{OH}$, with signal intensities increasing as the
 666 reaction time progressed (Fig. S10). It should be noted that EPR-based spin-trapping

667 methods have inherent limitations. For example, spectral overlap and background
668 signals may affect the resolution and accuracy of peak assignment. Furthermore,
669 certain short-lived or low-reactivity ROS may not be effectively captured by the
670 selected spin traps. Therefore, the reported ROS contributions should be interpreted as
671 semi-quantitative estimates rather than absolute concentrations

672 Then, a chemical probe method was employed to further quantify the
673 concentrations of $\cdot\text{OH}$ and $^1\text{O}_2$. Benzoic acid (BA) was used as the $\cdot\text{OH}$ probe
674 compound according to previously established protocol (Hu et al., 2025). Briefly, six
675 different concentration of BA (5, 10, 15, 20, 30, 40 and 50 μM) were added to
676 separate aliquots of the same extract. After illuminating for time t , the residual BA
677 concentration was monitored by UPLC-PDA. A linear regression of $-\ln[\text{BA}]/\ln[\text{BA}]_0$
678 versus reaction time t yielded the pseudo-first-order rate constant (k_{BA}) (Fig. 10 a, b).
679 By plotting the reciprocal ($1/k_{\text{BA}}$) against $[\text{BA}]$, the intercept was obtained (Fig. 10 c),
680 from which $[\text{OH}]_{\text{ss}}$, was determined by dividing the intercept by the second-order rate
681 constants $k_{\text{BA}, \text{OH}}$ (Lei et al., 2023). The $k_{\text{BA}, \text{OH}}$ is strongly dependent on pH value.
682 Under low pH conditions, benzoic acid predominantly exists in its molecular form
683 (BA), whereas at high pH it is mainly present as the deprotonated species (benzoate,
684 BA^-). These different forms exhibit distinct reactivity toward $\cdot\text{OH}$. According to the
685 literature (Arakaki et al., 2013), when $\text{pH} > 6$, BA^- is the dominant species, with a
686 rate constant $k_{\text{BA}^-, \text{OH}} = 6.0 \times 10^9 \text{ M}^{-1} \text{ s}^{-1}$; when $\text{pH} < 4$, the molecular form dominates,
687 with $k_{\text{BAOH}} = 1.8 \times 10^9 \text{ M}^{-1} \text{ s}^{-1}$. In this study, the initial pH values of coal and maize
688 samples were 6.79 and 5.83, therefore, $5.1 \times 10^9 \text{ M}^{-1} \text{ s}^{-1}$ (Lei et al., 2023) was
689 adopted to calculate the steady-state concentration of OH. The estimated $[\text{OH}]_{\text{ss}}$ were
690 $9.11 \times 10^{-14} \text{ M}$ and $8.58 \times 10^{-14} \text{ M}$ for coal and maize smoke extracts, respectively (Fig.

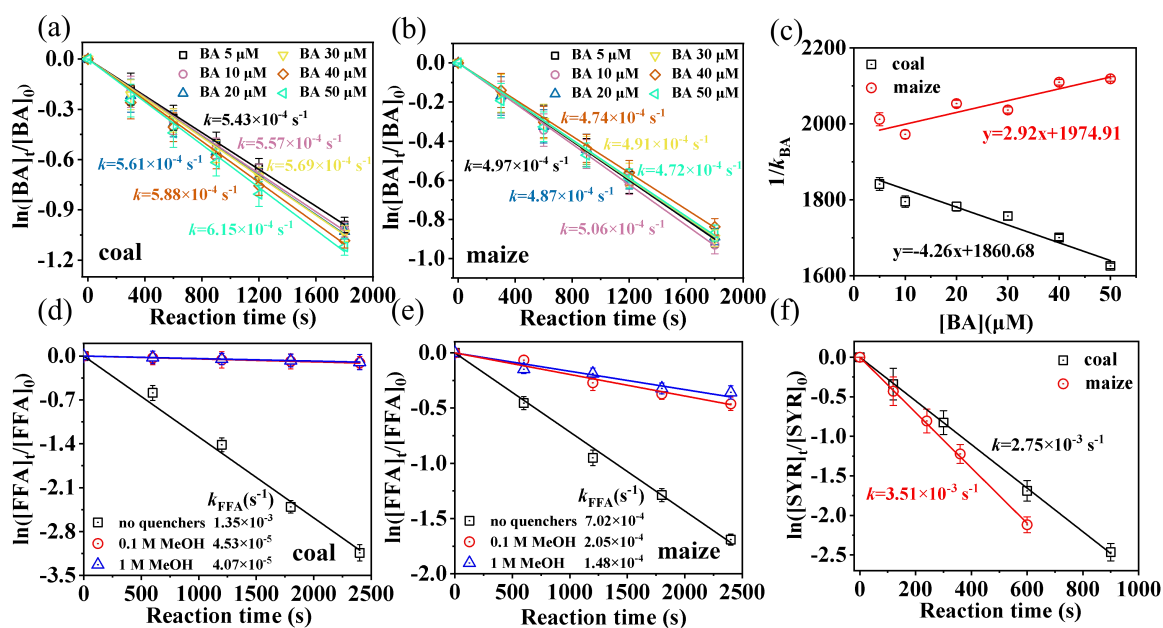
691 10)—values comparable to those typically observed in atmospheric cloud droplets
692 (Arakaki et al., 2013; Li et al., 2023).

693 The steady-state concentrations of $^1\text{O}_2$ and $^3\text{C}^*$ were also quantified by
694 monitoring the decay of furfuryl alcohol (FFA) and syringol (SYR) under
695 pseudo-first-order kinetics (Fig. 10 d-f), following previously established procedures
696 (Li et al., 2024). Considering the relatively high $\bullet\text{OH}$ concentration in the mixed
697 system, potential interference may occur when using FFA as a probe, since it can react
698 with both $\bullet\text{OH}$ ($k_{\text{FFA}, \text{OH}}=1.5\times 10^{10} \text{ M}^{-1} \text{ s}^{-1}$) and $^1\text{O}_2$ ($k_{\text{FFA}, ^1\text{O}_2}=1.2\times 10^8 \text{ M}^{-1} \text{ s}^{-1}$). To
699 eliminate this interference, excess methanol was added to completely quench $\bullet\text{OH}$
700 ($k_{\text{MeOH}, \text{OH}}=1.0\times 10^9 \text{ M}^{-1} \text{ s}^{-1}$) before employing FFA to determine the $^1\text{O}_2$ concentration.
701 The results (Fig. 10) showed that the $[^1\text{O}_2]_{\text{ss}}$ values were $3.48\times 10^{-13} \text{ M}$ and 1.8×10^{-12}
702 M for coal and maize smoke extracts, respectively, higher than that reported for 5
703 mgC L^{-1} of SOA extracts ($3\times 10^{-14} \text{ M}$) (Manfrin et al., 2019). Generally, $^1\text{O}_2$ was born
704 by triplets thus tightly linked to $^3\text{C}^*$. The significantly higher $^1\text{O}_2$ concentration
705 observed in maize smoke extracts—approximately six times that of coal smoke
706 extracts—indicates a greater abundance of triplet-state precursors in maize-derived
707 WSOM. Similarly, SYR was employed as a chemical probe due to its high reactivity
708 with triplets ($k_{\text{SYR}, ^3\text{C}^*}=3.9 \times 10^9 \text{ M}^{-1} \text{ s}^{-1}$) (Ma et al., 2023). Based on its
709 pseudo-first-order decay kinetics, the steady-state concentrations of $^3\text{C}^*$ in the maize
710 and coal systems were determined to be $9.0\times 10^{-13} \text{ M}$ and $7.05\times 10^{-13} \text{ M}$, respectively
711 (Fig. 11f).

712 The steady-state concentrations determined in our system are approximately one

713 order of magnitude higher than those reported in aqueous PM extracts illuminated
714 with 365 nm lamps (e.g., $\sim 10^{-13}$ M for triplets) (Bogler et al., 2022). Data from Ma et
715 al. (2024) also showed the concentrations of $\bullet\text{OH}$, $^1\text{O}_2$, and $^3\text{C}^*$ in $\text{PM}_{2.5}$ extracts range
716 from $(0.2\text{--}4.7) \times 10^{-15}$ M, $(0.7\text{--}45) \times 10^{-13}$ M, and $(0.03\text{--}7.9) \times 10^{-13}$ M, respectively.
717 This significant difference is mainly attributed to the addition of 10 mM H_2O_2 in our
718 experiments. Given an estimated average molecular weight of 300 g/mol for WSOM,
719 the resulting molar ratio of H_2O_2 to WSOM (15 mg C/L) is approximately 200:1. This
720 substantial excess of H_2O_2 provides a high concentration of $\bullet\text{OH}$, sufficient to
721 extensively oxidize WSOM and explaining why our $\bullet\text{OH}$ levels are orders of
722 magnitude greater than those in typical PM extracts (Ma et al., 2024).

723 Consequently, the degradation of WSOM in our system is predominantly driven
724 by $\bullet\text{OH}$ oxidation, with minor contributions from other reactive species. Furthermore,
725 the concentrations of $^1\text{O}_2$ and $^3\text{C}^*$ were also slightly higher than those in ambient PM
726 extracts (Ma et al., 2024), likely because our simulated combustion samples contained
727 higher levels of phenolic compounds and PAHs, which are known precursors for these
728 species.



729

730 **Fig. 10.** Loss of (a,b) BA, (d,e) FFA, (f) SYR and (c) plot of $1/k_{BA}$ and BA concentration

731 To elucidate the reaction mechanism, the role of different ROS in the photodecay
 732 and light absorbance of smoke extracts were examined. The absorption spectra of
 733 smoke extracts with and without 0.1 M methanol (α OH quencher) were compared
 734 (Fig. S11). A molar ratio of 2000:1(MeOH: WSOM) was employed, assuming an
 735 average molecular weight of 300 g/mol, to ensure complete scavenging OH given the
 736 comparable second-order rate constants of MeOH and WSOM with α OH (Liu-Kang
 737 et al., 2024). As shown in Fig. S11, absorbance decay rate decreased markedly,
 738 especially within the first hour, indicating that α OH play a dominant role in the
 739 photodacay of the extracts.

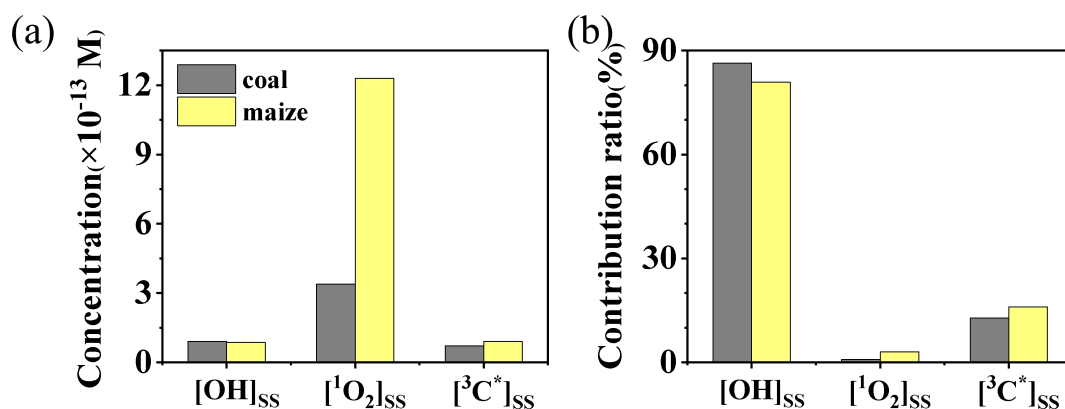
740 To further assess the contributions of individual ROS, comparative experiments
 741 were conducted under N_2 -, air-, and O_2 -saturated conditions. Under N_2 saturation,
 742 secondary oxidants such as $HO_2\cdot$ and $\cdot OH$ were largely excluded due to the absence
 743 of oxygen. The changes in WSOC indicate that direct photolysis in both smoke

744 extracts was much weaker than $\bullet\text{OH}$ oxidation. Under $\bullet\text{OH}$ oxidation, the WSOC
745 loss under N_2 -saturated conditions was much lower than that under O_2 - and
746 air-saturated conditions (Fig. S12), whereas in direct photolysis, the differences
747 among the three gas conditions were negligible (Fig. S13). This suggests that O_2 plays
748 a crucial role only for $\bullet\text{OH}$ oxidation.

749 Previous studies have reported that $^3\text{C}^*$ -initiated photooxidation of phenolic
750 compounds proceeds most rapidly under N_2 -saturated conditions (Lei et al., 2023). In
751 contrast, our results showed the fastest degradation under O_2 -saturated and the slowest
752 under N_2 , implying that $^3\text{C}^*$ is not the dominant oxidant in our system. This
753 conclusion is further supported by the comparable WSOC degradation observed for
754 coal and maize smoke extracts. Theoretically, if $^3\text{C}^*$ were the primary oxidant, maize
755 extracts would be expected to exhibit a much higher WSOC degradation owing to
756 their greater content of photosensitizers, as indicated by the higher lignin-like
757 compounds in maize (Section 3.3).

758 The relative importance of individual ROS in WSOM photodecay was evaluated
759 by multiplying their corresponding second-order rate constants with their steady-state
760 concentrations. Thus, we estimated the relative role in smoke WSOM photodecay.
761 Given that reaction rates of WSOC with O_3OH and $^3\text{C}^*$ were $3.8 \times 10^8 \text{ M}^{-1}\text{s}^{-1}$ and
762 $7.2 \times 10^7 \text{ M}^{-1}\text{s}^{-1}$, whereas $^1\text{O}_2$ reacts much more slowly ($10^5 \text{ M}^{-1}\text{s}^{-1}$) (Ma et al., 2024),
763 the contributions were calculated (Fig. 10b). For coal smoke extract, O_3OH , $^3\text{C}^*$, $^1\text{O}_2$
764 accounted for approximate 86.4%, 12.8% and 0.8% of the total oxidation, respectively.
765 A similar pattern was observed for maize smoke extracts (80.9%, 16.0% and 3.1%),

766 with the overall contribution order of $\alpha\text{OH} > {}^3\text{C}^* > {}^1\text{O}_2$. Although ${}^1\text{O}_2$ exhibited the
 767 highest steady-state concentration, its low reactivity limited its overall contribution,
 768 consistent with previous findings (Zhang et al., 2024). According to earlier reports
 769 (Tang et al., 2025), when the concentration of the BB-derived mixture reaches 12 mg
 770 C/L, the concentration of photosensitizers in solution can exceed several millimoles.
 771 Therefore, ${}^3\text{C}^*$ also plays an important and non-negligible role in the
 772 photodegradation of both smoke WSOM.



773

774 **Fig. 11.** ROS steady-state contribution and their contribution to WSOM photodecay

775 Surely, different H_2O_2 concentrations might influence the relative role of ROS. To
 776 assess this effect, we examined the ROS concentrations and their contributions under
 777 five different H_2O_2 levels (0.5, 1, 3, 5, and 10 mM). The results are presented in Table
 778 S5. As shown in Table S5, increasing the H_2O_2 dosage leads to higher $\bullet\text{OH}$
 779 concentrations and relative contributions, accompanied by a corresponding decrease
 780 in the contribution of triplet excited states (${}^3\text{C}^*$). The measured $\bullet\text{OH}$ concentrations
 781 generally fall within a relatively narrow range under five different H_2O_2 concentration,
 782 with average values of $(0.7 - 9.1) \times 10^{-14}$ M and $(1.3 - 8.3) \times 10^{-14}$ M, for coal and maize
 783 smoke WSOM, respectively. Specifically, we also noted that the ${}^1\text{O}_2$ contribution is

784 only weakly affected by the H₂O₂ concentration. Given that this study mainly focuses
785 on the role of •OH, all subsequent experiments were conducted at a relatively high
786 H₂O₂ concentration. While additional experiments at varying H₂O₂ concentrations
787 would provide valuable quantitative constraints on these processes, they are beyond
788 the scope of the present study.

789 **3.6.2 Photochemical transformation of smoke extracts**

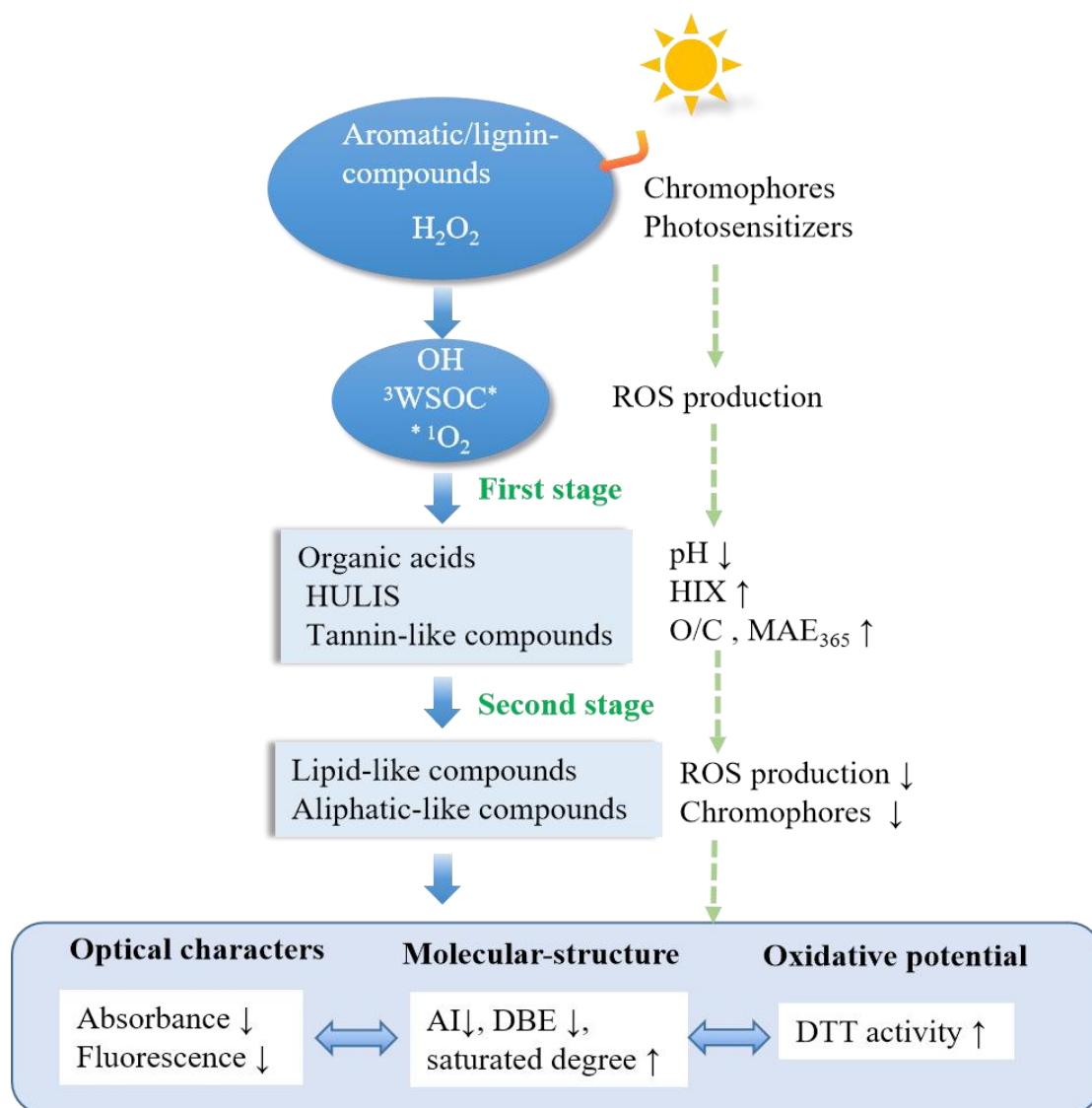
790 By introducing extra H₂O₂, the •OH concentration and its role in the photoaging
791 of both smoke extracts were altered. The added •OH accounts for a major fraction of
792 the total oxidants in both systems, thereby influencing the overall optical properties
793 and chemical composition. Based on the ROS measurements and molecular analyses,
794 a conceptual mechanism for the aqueous photooxidation of both smoke extracts is
795 proposed (Fig. 12). Upon irradiation, photosensitizers in WSOM absorb photons and
796 form triplet excited states (³PS*), which transfer energy or electrons to dissolved O₂,
797 generating various ROS (¹O₂, O₂^{•-}, •HO₂, and •OH). These reactive species initiate and
798 propagate oxidation processes, thereby modifying the chemical composition and
799 optical properties of WSOM.

800 In the first stage, abundant •OH rapidly attacks electron-rich aromatic and
801 conjugated structures, cleaving C=C and C–O bonds and causing a sharp decrease in
802 WSOC and light absorbance. Meanwhile, both ³Sen* and ¹O₂ selectively oxidizes
803 lignin-like compounds, forming oxygenated intermediates such as carbonyls, and
804 carboxylic acids, resulting in gradual decrease in solution pH (Fig. S7) and increase in
805 O/C.

806 As the reaction proceeds, the depletion of aromatic chromophores suppresses
807 further ROS formation, consistent with the observed decline in DTT activity. FT-ICR
808 MS analysis further supports this evolution, revealing a shift from high H/C, low O/C
809 aromatic compounds toward lipid- or aliphatic-like species.

810 Interestingly, although total WSOC decreased with aging, WSOC-normalized
811 DTT activity increased due to probable highly DTT active species (e.g., quinone-like
812 species). Similar trends have been observed in BBOA-WSOC OH-photooxidation
813 aging, where oxidative potential decreased at the initial period (~ 5 h) despite WSOC
814 mass loss (Wong et al., 2019).

815 Overall, the aqueous photooxidation of two smoke extracts involves a dynamic
816 interplay among $\bullet\text{OH}$, $^3\text{C}^*$, and $^1\text{O}_2$. The early stage is dominated by $\bullet\text{OH}$ -driven
817 degradation of chromophores, followed by secondary formation of oxygenated,
818 potentially more toxic species through $^1\text{O}_2$ and triplet-state reactions. These processes
819 jointly govern the chemical evolution, light-absorbing behavior, and oxidative
820 potential of WSOM during photochemical aging.



821
822 **Fig. 12.** Proposed photochemical transformation pathways for two smoke extracts

823 Next, by integrating FT-ICR MS and ROS analyses, we further compared the
824 molecular transformation mechanisms of the two types of smoke. Table S6 and S7 list
825 the top 10 most abundant compounds identified by FT-ICR MS before photolysis and
826 after 11 h and 23 h of irradiation, together with their DBE values, molecular formulas,
827 inferred functional groups, and FT-ICR MS classifications.

828 Fresh coal-derived WSOM is mainly composed of CHO and CHOS compounds,
829 including organosulfates (e.g., C₁₂H₂₆O₄S, C₁₇H₂₈O₃S, and C₁₈H₃₀O₃S), aromatic
830 oxygenated species (e.g., C₁₂H₁₂O₅ and C₁₃H₁₄O₅), and aliphatic compounds (e.g.,
831 C₁₈H₃₆O₃). During photochemical processing, only limited transformation is observed

832 among the top 10 compounds, although partial conversion of lignin-like structures
833 into lipid-like species occurs. Several molecular formulas (e.g., $C_{17}H_{28}O_3S$,
834 $C_{18}H_{30}O_3S$, $C_{16}H_{32}O_2$, and $C_{18}H_{36}O_3$) persist before and after 11 h of irradiation,
835 indicating their relative resistance to photochemical degradation. Consequently, the
836 average molecular weight of coal-derived WSOM exhibits only minor variation
837 during oxidation.

838 The transformation of coal smoke WSOM can be summarized by three main
839 pathways. First, aromatic compounds (e.g., $C_{12}H_{12}O_5$ and $C_{13}H_{14}O_5$)
840 undergo $\bullet OH$ -driven oxidation and tend to break down into smaller molecules,
841 contributing to the loss of aromatic structures. Second, aliphatic compounds (e.g.,
842 $C_{18}H_{36}O_3$) are oxidized via $\bullet OH$ -initiated functionalization, forming more stable
843 oxygenated fatty acid-like products such as $C_{16}H_{32}O_2$ and $C_{18}H_{36}O_2$, along with
844 partially oxidized intermediates (e.g., $C_{18}H_{34}O_3$). Third, CHOS compounds exhibit
845 partial stability, with long-chain organosulfates (e.g., $C_{18}H_{30}O_3S$) persisting
846 throughout the oxidation process.

847 In contrast, maize smoke WSOM shows distinctly different behavior. The fresh
848 sample was dominated by lignin-like compounds, such as $C_9H_{10}O_3$ and $C_9H_8O_3$,
849 reflecting the prevalence of aromatic structures derived from biomass combustion.
850 During aqueous-phase oxidation, these compounds undergo extensive transformation
851 driven primarily by $\bullet OH$ attack, including hydrogen abstraction and electrophilic
852 addition to aromatic rings. These reactions promote hydroxylation, denitration, and
853 subsequent ring-opening processes, leading to the formation of highly oxygenated and
854 lower-molecular-weight products. As a result, both aromaticity and average molecular
855 weight decrease significantly. This trend is supported by the appearance of highly
856 oxygenated species (e.g., $C_9H_{10}O_7$ and $C_9H_{18}O_6$ at 11 h), which shift toward higher

857 O/C ratios in the Van Krevelen space. Meanwhile, lignin-like compounds are
858 progressively transformed into lipid-like, tannin-like, and aliphatic species. Notably,
859 the top 10 products at 11 h and 23 h exhibit strong similarity (e.g., $C_{14}H_{22}O$, $C_{16}H_{32}O_2$,
860 $C_{18}H_{36}O_2$, and $C_{12}H_{26}O_4S$), suggesting the formation of relatively stable oxidation
861 products at later stages.

862 Overall, these results demonstrate that maize smoke undergoes more extensive
863 oxidation, characterized by pronounced aromatic degradation and molecular
864 fragmentation, whereas coal smoke exhibits higher chemical stability, with limited
865 molecular transformation and a greater persistence of initial compounds.

866 **4 Conclusions**

867 This study systematically investigated the aqueous-phase $\bullet OH$ -driven
868 photodegradation of coal and maize smoke extracts, providing molecular-level
869 insights into their molecular and optical evolution. EEM-PARAFAC resolved one
870 humic-like and two protein-like components, revealing distinct temporal patterns
871 between coal and maize systems. FT-ICR MS further showed that both samples were
872 dominated by CHO and CHON compounds, with maize smoke enriched in CHON
873 species and coal smoke containing a higher fraction of sulfur-containing compounds.

874 Aqueous photooxidation led to increased molecular saturation and reduced
875 aromaticity, as evidenced by declining DBE and AI values. Lignin-like compounds
876 were progressively depleted, accompanied by an increase in lipid- and aliphatic-like
877 species, suggesting the breakdown of conjugated structures and the formation of more
878 saturated, oxygenated products. These transformations reduced chromophoric content
879 through double-bond cleavage and aromatic ring opening, resulting in decreased light
880 absorption and fluorescence.

881 The contributions of ROS to photodegradation followed the order $\bullet\text{OH} > {}^3\text{C}^* >$
882 ${}^1\text{O}_2$, highlighting the dominant role of $\bullet\text{OH}$ in aqueous-phase processing. Despite
883 these common trends, distinct photochemical pathways were observed. Maize-derived
884 WSOM exhibited more rapid oxidation during the early stage, likely driven by
885 OH-functionalization reactions, whereas coal-derived WSOM showed greater
886 compositional stability. Mechanistically, ROS promoted the conversion of lignin-like
887 aromatics into highly oxygenated products via hydroxylation and ring-opening, while
888 lipid-like compounds undergo functionalization and fragmentation. Secondary
889 reactions with sulfate lead to the formation of organosulfates.

890 HR-AMS results confirmed the formation of low-molecular-weight carboxylic
891 acids (e.g., oxalate), accompanied by decreasing pH and increasing oxidation state of
892 aqSOA, particularly in maize systems. Although total WSOC decreased during
893 photodegradation, the WSOC-normalized oxidative potential increased, as indicated
894 by enhanced DTT consumption, likely due to the formation of nitrogen-containing
895 compounds in coal smoke and reactive quinones in maize smoke. Furthermore,
896 maize-derived aqSOA exhibited higher oxidation levels, whereas coal smoke
897 produced higher aqSOA mass yields.

898 Overall, aqueous-phase photochemical processing simultaneously weakens
899 optical properties and enhances chemical reactivity. From an atmospheric perspective,
900 cloud and fog processing can substantially modify the properties of smoke-derived
901 WSOM. The transformation of aromatic chromophores into more saturated products
902 reduces brown carbon light absorption, potentially weakening its direct radiative
903 forcing. At the same time, the formation of highly oxidized and redox-active species
904 may enhance aerosol oxidative potential and toxicity. These findings underscore the
905 importance of incorporating aqueous-phase transformations into atmospheric models

906 to more accurately assess the climate and air quality impacts of emissions from
907 different fuel sources.

908 **Data availability.**

909 All data used in this study are available upon request.

910 **Author contributions.**

911 ZY and XG developed the research objectives and designed the experiments. DH
912 and XH set up the combustion sampling apparatus and collected samples. DH and QC
913 conducted the photochemistry experiments and analyzed the data with the help of XH.
914 ZY prepared the manuscript with contributions from all co-authors. ZY and XG
915 provided supervision and guidance during the experiments and writing.

916 **Competing interests.**

917 The contact author has declared that none of the authors has any competing interests.

918 **Acknowledgements.**

919 We appreciate the comments and efforts of the two anonymous reviewers.

920 **Financial support.**

921 The authors acknowledge support from the Natural Science Foundation of
922 Jiangsu Province (BK20221405) and National foreign expert project (H20240368).

923 We are also thankful for funding support from Natural Science Foundation of China
924 (22361162668), Natural Science Foundation of the Jiangsu Higher Education
925 Institutions of China (25KJD170010), and the Postgraduate Research & Practice
926 Innovation Program of Jiangsu Province (SJCX24_1808).

927 **References**

928 Arakaki, T., Anastasio, C., Kuroki, Y., Nakajima, H., Okada, K., Kotani, Y., Handa, D., Azechi,
929 S., Kimura, T., Tshako, A., and Miyagi, Y.: A general scavenging rate constant for reaction of

930 hydroxyl radical with organic carbon in atmospheric waters, *Environ. Sci. Technol.*, 47,
931 8196–8203, <https://doi.org/10.1021/es401927b>, 2013.

932 Arciva, S., Niedek, C., Mavis, C., Yoon, M., Sanchez, M. E., Zhang, Q., and Anastasio, C.:
933 Aqueous ·OH oxidation of highly substituted phenols as a source of secondary organic aerosol,
934 *Environ. Sci. Technol.*, 56, 9959–9967, <https://doi.org/10.1021/acs.est.2c02225>, 2022.

935 Arciva, S., Ma, L., Mavis, C., Guzman, C., and Anastasio, C.: Formation and loss of light
936 absorbance by phenolic aqueous SOA by OH and an organic triplet excited state, *Atmos. Chem.*
937 *Phys.*, 24, 4473–4485, <https://doi.org/10.5194/acp-24-4473-2024>, 2024.

938 Bogler, S., Daellenbach, K. R., Bell, D. M., Prévôt, A. S. H., El Haddad, I., and
939 Borduas-Dedekind, N.: Singlet oxygen seasonality in aqueous PM₁₀ is driven by biomass
940 burning and anthropogenic secondary organic aerosol, *Environ. Sci. Technol.*, 56, 15389–15397,
941 <https://doi.org/10.1021/acs.est.2c04554>, 2022.

942 Cao, T., Xu, C., Chen, H., Song, J., Li, J., Song, H., Jiang, B., Zhong, Y., and Peng, P.: Molecular
943 insight into aqueous-phase photolysis and photooxidation of water-soluble organic matter
944 emitted from biomass burning and coal combustion, *Atmos. Chem. Phys.*, 25, 11597–11610,
945 <https://doi.org/10.5194/acp-25-11597-2025>, 2025.

946 Chen, Q., Wang, M., Wang, Y., Zhang, L., Li, Y., and Han, Y.: Oxidative potential of
947 water-soluble matter associated with chromophoric substances in PM_{2.5} over Xi'an, China,
948 *Environ. Sci. Technol.*, 53, 8574–8584, <https://doi.org/10.1021/acs.est.9b01976>, 2019.

949 Chen, W., Zhang, H., Xu, S., Jia, H., Qi, Z., Farooq, U., Wang, Z., and Dai, Q.: New insights into
950 the molecular characteristics-dependent light absorption variation of water-soluble organic
951 matter in biomass burning smoke, *Atmos. Res.*, 316, 107951,
952 <https://doi.org/10.1016/j.atmosres.2025.107951>, 2025.

953 Cook, R. D., Lin, Y.-H., Peng, Z., Boone, E., Chu, R. K., Dukett, J. E., Gunsch, M. J., Zhang, W.,
954 Tolic, N., Laskin, A., and Pratt, K. A.: Biogenic, urban, and wildfire influences on the
955 molecular composition of dissolved organic compounds in cloud water, *Atmos. Chem. Phys.*,
956 17, 15167–15180, <https://doi.org/10.5194/acp-17-15167-2017>, 2017.

957 Fan, X., Wei, S., Zhu, M., Song, J., and Peng, P.: Comprehensive characterization of humic-like
958 substances in smoke PM_{2.5} emitted from the combustion of biomass materials and fossil fuels,
959 *Atmos. Chem. Phys.*, 16, 13321–13340, <https://doi.org/10.5194/acp-16-13321-2016>, 2016.

960 Fan, X., Li, M., Cao, T., Cheng, C., Li, F., Xie, Y., Wei, S., Song, J., and Peng, P.: Optical
961 properties and oxidative potential of water- and alkaline-soluble brown carbon in smoke
962 particles emitted from laboratory simulated biomass burning, *Atmos. Environ.*, 194, 48–57,
963 <https://doi.org/10.1016/j.atmosenv.2018.09.025>, 2018.

964 Fan, X., Xie, S., Yu, X., Cheng, A., Chen, D., Ji, W., Liu, X., Song, J., and Peng, P.:
965 Molecular-level transformations of biomass burning-derived water-soluble organic carbon
966 during dark aqueous OH oxidation: Insights from absorption, fluorescence, high-performance

967 size exclusion chromatography and high-resolution mass spectrometry analysis, *Sci. Total*
968 *Environ.*, 912, 169290, <https://doi.org/10.1016/j.scitotenv.2023.169290>, 2024.

969 Fang, Z., Lai, A., Cai, D., Li, C., Carmieli, R., Chen, J., Wang, X., and Rudich, Y.: Secondary
970 organic aerosol generated from biomass burning emitted phenolic compounds: Oxidative
971 potential, reactive oxygen species, and cytotoxicity, *Environ. Sci. Technol.*, 58, 8194–8206,
972 <https://doi.org/10.1021/acs.est.3c09903>, 2024.

973 Gerritz, L., Wei, J., Fang, T., Wong, C., Klodt, A. L., Nizkorodov, S. A., and Shiraiwa, M.:
974 Reactive oxygen species formation and peroxide and carbonyl decomposition in aqueous
975 photolysis of secondary organic aerosols, *Environ. Sci. Technol.*, 58, 4716–4726,
976 <https://doi.org/10.1021/acs.est.3c08662>, 2024.

977 Go, B. R., Li, Y. J., Huang, D. D., Wang, Y., and Chan, C. K.: Comparison of aqueous secondary
978 organic aerosol (aqSOA) product distributions from guaiacol oxidation by non-phenolic and
979 phenolic methoxybenzaldehydes as photosensitizers in the absence and presence of ammonium
980 nitrate, *Atmos. Chem. Phys.*, 23, 2859–2875, <https://doi.org/10.5194/acp-23-2859-2023>, 2023.

981 Go, B. R., Li, Y. J., Huang, D. D., and Chan, C. K.: Aqueous-phase photoreactions of mixed
982 aromatic carbonyl photosensitizers yield more oxygenated, oxidized, and less light-absorbing
983 secondary organic aerosol (SOA) than single systems, *Environ. Sci. Technol.*, 58, 7924–7936,
984 <https://doi.org/10.1021/acs.est.3c10199>, 2024.

985 Hems, R. F., Schnitzler, E. G., Bastawrous, M., Soong, R., Simpson, A. J., and Abbatt, J. P. D.:
986 Aqueous photoreactions of wood smoke brown carbon, *ACS Earth Space Chem.*, 4, 1149–1160,
987 <https://doi.org/10.1021/acsearthspacechem.0c00117>, 2020.

988 Hu, D., Ye, Z., Wang, Z., Topping, D., Aruffo, E., Wang, H., and Ge, X.: Kinetics and quantum
989 yield of photosensitized reactions from substituted phenols via chemical probe approach, *Atmos.*
990 *Environ.*, 360, 121419, <https://doi.org/10.1016/j.atmosenv.2025.121419>, 2025a.

991 Hu, D., Wang, Z., Aruffo, E., Dai, X., Zhao, Z., and Ye, Z.: Kinetics of different substituted
992 Phenolic compounds' aqueous OH oxidation in atmosphere, *Atmosphere*, 16,
993 <https://doi.org/10.3390/atmos16050567>, 2025b.

994 Huang, Y., Li, X., Huang, D. D., Lei, R., Zhou, B., Zhang, Y., and Ge, X.:
995 Machine-learning-assisted chemical characterization and optical properties of atmospheric
996 brown carbon in Nanjing, China, *Atmos. Chem. Phys.*, 25, 7619–7645,
997 <https://doi.org/10.5194/acp-25-7619-2025>, 2025.

998 Jiang, H. and Jang, M.: Dynamic oxidative potential of atmospheric organic aerosol under ambient
999 sunlight, *Environ. Sci. Technol.*, 52, 7496–7504, <https://doi.org/10.1021/acs.est.8b00148>, 2018.

1000 Jiang, W., Misovich, M. V., Hettiyadura, A. P. S., Laskin, A., McFall, A. S., Anastasio, C., and
1001 Zhang, Q.: Photosensitized reactions of a phenolic carbonyl from wood combustion in the
1002 aqueous phase—Chemical evolution and light absorption properties of aqSOA, *Environ. Sci.*
1003 *Technol.*, <https://doi.org/10.1021/acs.est.0c07581>, 2021.

- 1004 Jiang, W., Niedek, C., Anastasio, C., and Zhang, Q.: Photoaging of phenolic secondary organic
1005 aerosol in the aqueous phase: evolution of chemical and optical properties and effects of
1006 oxidants, *Atmos. Chem. Phys.*, 23, 7103–7120, <https://doi.org/10.5194/acp-23-7103-2023>,
1007 2023.
- 1008 Lei, R., Sha, Y., Meng, H., Huang, Y., Ye, J., Huang, D. D., Zhang, Y., Wu, Y., Li, Y., and Ge, X.:
1009 Aqueous phase photolysis of 4-nitrocatechol: Reaction kinetics, evolutions of chemical
1010 composition, light absorption and oxidation potential, *Atmos. Environ.*, 343, 120981,
1011 <https://doi.org/10.1016/j.atmosenv.2024.120981>, 2025.
- 1012 Lei, Y., Yu, Y., Lei, X., Liang, X., Cheng, S., Ouyang, G., and Yang, X.: Assessing the use of
1013 probes and quenchers for understanding the reactive species in advanced oxidation processes,
1014 *Environ. Sci. Technol.*, 57, 5433–5444, <https://doi.org/10.1021/acs.est.2c09338>, 2023.
- 1015 Lei, Y., Lei, X., Tian, G., Yang, J., Huang, D., Yang, X., Chen, C., and Zhao, J.: Optical variation
1016 and molecular transformation of brown carbon during oxidation by $\text{NO}_3\cdot$ in the aqueous phase,
1017 *Environ. Sci. Technol.*, 58, 3353–3362, <https://doi.org/10.1021/acs.est.3c08726>, 2024.
- 1018 Leresche, F., Salazar, J. R., Pfotenhauer, D. J., Hannigan, M. P., Majestic, B. J., and Rosario-Ortiz,
1019 F. L.: Photochemical aging of atmospheric particulate matter in the aqueous phase, *Environ. Sci.*
1020 *Technol.*, 55, 13152–13163, <https://doi.org/10.1021/acs.est.1c00978>, 2021.
- 1021 Li, F., Tsona, N. T., Li, J., and Du, L.: Aqueous-phase oxidation of syringic acid emitted from
1022 biomass burning: Formation of light-absorbing compounds, *Sci. Total Environ.*, 765, 144239,
1023 <https://doi.org/10.1016/j.scitotenv.2020.144239>, 2021.
- 1024 Li, F., Zhou, S., Du, L., Zhao, J., Hang, J., and Wang, X.: Aqueous-phase chemistry of
1025 atmospheric phenolic compounds: A critical review of laboratory studies, *Sci. Total Environ.*,
1026 856, 158895, <https://doi.org/10.1016/j.scitotenv.2022.158895>, 2023.
- 1027 Li, F., Zhou, S., Zhao, J., Hang, J., Lu, H., Li, X., Gao, M., Li, Y., and Wang, X.: Aqueous
1028 photosensitization of syringaldehyde: Reactivity, effects of environmental factors, and
1029 formation of brown carbon products, *ACS Earth Space Chem.*, 8, 1193–1203,
1030 <https://doi.org/10.1021/acsearthspacechem.4c00004>, 2024a.
- 1031 Li, L., Han, Y., Li, J., Lin, Y., Zhang, X., Wang, Q., and Cao, J.: Effects of photochemical aging
1032 on the molecular composition of organic aerosols derived from agricultural biomass burning in
1033 whole combustion process, *Sci. Total Environ.*, 946, 174152,
1034 <https://doi.org/10.1016/j.scitotenv.2024.174152>, 2024b.
- 1035 Lin, P., Aiona, P. K., Li, Y., Shiraiwa, M., Laskin, J., Nizkorodov, S. A., and Laskin, A: Molecular
1036 characterization of brown carbon in biomass burning aerosol particles, *Environ. Sci. Technol.*, 50,
1037 11815–11824, <https://doi.org/10.1021/acs.est.6b03024>, 2016.
- 1038 Li, X., Tao, Y., Zhu, L., Ma, S., Luo, S., Zhao, Z., Sun, N., Ge, X., and Ye, Z.: Optical and
1039 chemical properties and oxidative potential of aqueous-phase products from OH and

- 1040 $^3\text{C}^*$ -initiated photooxidation of eugenol, *Atmos. Chem. Phys.*, 22, 7793–7814,
1041 <https://doi.org/10.5194/acp-22-7793-2022>, 2022.
- 1042 Liu-Kang, C., Sokolova, A., Gong, Y., Fahy, W. D., Peng, H., and Abbatt, J. P. D.: Light exposure
1043 of wood smoke aerosol: Connecting optical properties, oxidation, radical formation, and
1044 chemical composition, *ACS EST Air*, 1, 273–282, <https://doi.org/10.1021/acsestair.3c00063>,
1045 2024.
- 1046 Ma, L., Worland, R., Jiang, W., Niedeck, C., Guzman, C., Bein, K. J., Zhang, Q., and Anastasio, C.:
1047 Predicting photooxidant concentrations in aerosol liquid water based on laboratory extracts of
1048 ambient particles, *Atmos. Chem. Phys.*, 23, 8805–8821,
1049 <https://doi.org/10.5194/acp-23-8805-2023>, 2023.
- 1050 Ma, L., Worland, R., Heinlein, L., Guzman, C., Jiang, W., Niedeck, C., Bein, K. J., Zhang, Q., and
1051 Anastasio, C.: Seasonal variations in photooxidant formation and light absorption in aqueous
1052 extracts of ambient particles, *Atmos. Chem. Phys.*, 24, 1–21,
1053 <https://doi.org/10.5194/acp-24-1-2024>, 2024.
- 1054 Mahamuni, G., Rutherford, J., Davis, J., Molnar, E., Posner, J. D., Seto, E., Korshin, G., and
1055 Novosselov, I.: Excitation–emission matrix spectroscopy for analysis of chemical composition
1056 of combustion generated particulate matter, *Environ. Sci. Technol.*, 54, 8198–8209,
1057 <https://doi.org/10.1021/acs.est.0c01110>, 2020.
- 1058 Manfrin, A., Nizkorodov, S. A., Malecha, K. T., Getzinger, G. J., McNeill, K., and
1059 Borduas-Dedekind, N.: Reactive oxygen species production from secondary organic aerosols:
1060 The importance of singlet oxygen, *Environ. Sci. Technol.*, 53, 8553–8562,
1061 <https://doi.org/10.1021/acs.est.9b01609>, 2019.
- 1062 Ning, C., Tang, Y., Sun, S., Wang, D., and Gao, Y.: Molecular level characteristics and sources of
1063 rainwater water-soluble organic matter in different regions of China by FT-ICR MS, *Atmos.*
1064 *Environ.*, 350, 121175, <https://doi.org/10.1016/j.atmosenv.2025.121175>, 2025.
- 1065 Song, J., Li, M., Jiang, B., Wei, S., Fan, X., and Peng, P.: Molecular characterization of
1066 water-soluble humic like substances in smoke particles emitted from combustion of biomass
1067 materials and coal using ultrahigh-resolution electrospray ionization Fourier Transform Ion
1068 Cyclotron Resonance Mass Spectrometry, *Environ. Sci. Technol.*, 52, 2575–2585,
1069 <https://doi.org/10.1021/acs.est.7b06126>, 2018.
- 1070 Tang, J., Li, J., Su, T., Han, Y., Mo, Y., Jiang, H., Cui, M., Jiang, B., Chen, Y., Tang, J., Song, J.,
1071 Peng, P., and Zhang, G.: Molecular compositions and optical properties of dissolved brown
1072 carbon in biomass burning, coal combustion, and vehicle emission aerosols illuminated by
1073 excitation–emission matrix spectroscopy and Fourier transform ion cyclotron resonance mass
1074 spectrometry analysis, *Atmos. Chem. Phys.*, 20, 2513–2532,
1075 <https://doi.org/10.5194/acp-20-2513-2020>, 2020.
- 1076 Tang, R., Ma, J., Zhang, R., Cui, W., Qin, Y., Chu, Y., Qin, Y., Vogel, A. L., and Chan, C. K.:
1077 Enhanced sulfate formation in mixed biomass burning and sea-salt interactions mediated by

1078 photosensitization: effects of chloride, nitrogen-containing compounds, and atmospheric aging,
1079 *Atmos. Chem. Phys.*, 25, 425–439, <https://doi.org/10.5194/acp-25-425-2025>, 2025.

1080 Tomaz, S., Cui, T., Chen, Y., Sexton, K. G., Roberts, J. M., Warneke, C., Yokelson, R. J., Surratt,
1081 J. D., and Turpin, B. J.: Photochemical cloud processing of primary wildfire emissions as a
1082 potential source of secondary organic aerosol, *Environ. Sci. Technol.*, 52, 11027–11037,
1083 <https://doi.org/10.1021/acs.est.8b03293>, 2018.

1084 Verma, V., Rico-Martinez, R., Kotra, N., King, L., Liu, J., Snell, T. W., and Weber, R. J.:
1085 Contribution of water-soluble and insoluble components and their hydrophobic/hydrophilic
1086 subfractions to the reactive oxygen species-generating potential of fine ambient aerosols,
1087 *Environ. Sci. Technol.*, 46, 11384–11392, <https://doi.org/10.1021/es302484r>, 2012.

1088 Vione, D., Albinet, A., Barsotti, F., Mekic, M., Jiang, B., Minero, C., Brigante, M., and
1089 Gligorovski, S.: Formation of substances with humic-like fluorescence properties, upon
1090 photoinduced oligomerization of typical phenolic compounds emitted by biomass burning,
1091 *Atmos. Environ.*, 206, 197–207, <https://doi.org/10.1016/j.atmosenv.2019.03.005>, 2019.

1092 Wang, H., Zheng, N., Du, H., Chen, Z., Sha, H., Zhou, H., and Ye, Z.: Microheterogeneous
1093 photogeneration of hydroxyl radical in sunlit dissolved black carbon solution, *J. Hazard. Mater.*,
1094 498, 139840, <https://doi.org/10.1016/j.jhazmat.2025.139840>, 2025.

1095 Wang, J. and Wang, S.: Reactive species in advanced oxidation processes: Formation, identification
1096 and reaction mechanism, *Chem. Eng. J.*, 401, 126158, <https://doi.org/10.1016/j.cej.2020.126158>, 2020.

1098 Wang, X., Hayeck, N., Brüggemann, M., Yao, L., Chen, H., Zhang, C., Emmelin, C., Chen, J.,
1099 George, C., and Wang, L.: Chemical characteristics of organic aerosols in Shanghai: A study by
1100 ultrahigh-performance liquid chromatography coupled with orbitrap mass spectrometry, *J.*
1101 *Geophys. Res. Atmos.*, 122, 11,703–11,722, <https://doi.org/10.1002/2017JD026930>, 2017.

1102 Wong, J. P. S., Nenes, A., and Weber, R. J.: Changes in light absorptivity of molecular weight
1103 separated brown carbon due to photolytic aging, *Environ. Sci. Technol.*, 51, 8414–8421,
1104 <https://doi.org/10.1021/acs.est.7b01739>, 2017.

1105 Wong, J. P. S., Tsagkaraki, M., Tsiotra, I., Mihalopoulos, N., Violaki, K., Kanakidou, M., Sciare,
1106 J., Nenes, A., and Weber, R. J.: Effects of atmospheric processing on the oxidative potential of
1107 biomass burning organic aerosols, *Environ. Sci. Technol.*, 53, 6747–6756,
1108 <https://doi.org/10.1021/acs.est.9b01034>, 2019.

1109 Wu, G., Fu, P., Ram, K., Song, J., Chen, Q., Kawamura, K., Wan, X., Kang, S., Wang, X., Laskin,
1110 A., and Cong, Z.: Fluorescence characteristics of water-soluble organic carbon in atmospheric
1111 aerosol, *Environ. Pollut.*, 268, 115906, <https://doi.org/10.1016/j.envpol.2020.115906>, 2021.

1112 Yang, N., Wang, J., Jacob, D. J., Ye, J., Sheng, M., Niu, M., Qin, Y., Ge, X., Sun, Y., Wang, Z.,
1113 Wang, Y., Wu, F., Liu, C.-Q., George, C., and Fu, P.: Aqueous production of sulfur-containing

- 1114 aerosols from nitroaromatic compounds and SO₂ in wintertime urban haze, *Sci. Bull.*, 70,
1115 1846–1855, <https://doi.org/10.1016/j.scib.2025.03.013>, 2025.
- 1116 Ye, Z., Hu, D., Wang, Z., Wang, H., and Ge, X.: Aqueous photochemical aging of water-soluble
1117 smoke particles from crop straws burning, *Atmos. Environ.*, 340, 120897,
1118 <https://doi.org/10.1016/j.atmosenv.2024.120897>, 2025.
- 1119 Zhang, H., Wu, L., Qian, W., Ni, J., Wei, R., Qi, Z., and Chen, W.: Spectral characteristics of
1120 dissolved organic carbon derived from biomass-pyrogenic smoke (SDOC) in the aqueous
1121 environment and its solubilization effect on hydrophobic organic pollutants, *Water Res.*, 203,
1122 117515, <https://doi.org/10.1016/j.watres.2021.117515>, 2021.
- 1123 Zhang, J., Shrivastava, M., Ma, L., Jiang, W., Anastasio, C., Zhang, Q., and Zelenyuk, A.:
1124 Modeling novel aqueous particle and cloud chemistry processes of biomass burning phenols
1125 and their potential to form secondary organic aerosols, *Environ. Sci. Technol.*, 58, 3776–3786,
1126 <https://doi.org/10.1021/acs.est.3c07762>, 2024.
1127